A&A 466, 215–228 (2007)
DOI: 10.1051/0004-6361:20054245

Astronomy & Astrophysics

Methanol as a diagnostic tool of interstellar clouds⋆,⋆⋆

II. Modelling high-mass protostellar objects

S. Leurini, P. Schilke, F. Wyrowski, and K. M. Menten

Max-Planck-Institut für Radioastronomie, Auf dem Hügel 69, 53121 Bonn, Germany
e-mail: [sleurini;schilke;wyrowski;kmenten]@mpifr-bonn.mpg.de

Received 23 September 2005 / Accepted 5 January 2007

ABSTRACT

Context. Fundamental properties of interstellar clouds must be known to investigate the initial conditions of star formation within them and the interaction of newly formed stars with their environment. Methanol has proven to be useful to probe densities and temperatures of various environments within interstellar clouds.
Aims. We aim to explore the potential of methanol as a tracer molecule for regions in which high-mass stars are forming or have recently formed, in particular so-called high-mass protostellar objects (HMPOs) and infrared dark clouds (IRDCs).
Methods. We present and analyse multi-frequency centimetre and (sub)millimetre single-dish observations of methanol toward a sample of 13 sources that are in the poorly understood earliest phases of evolution of high-mass stars (HMPOs and IRDCs). For each source in our sample, we derive physical parameters such as the kinetic temperature, the spatial density. and the methanol column density. We apply our large velocity gradient modelling and fitting technique that involves fitting a synthetic spectrum to all the measured lines simultaneously.
Results. In several sources, we find that more than one physical component is necessary to fit the spectra; moreover, broad non-Gaussian linewidths suggest outflows in many sources from both the IRDC and the HMPO subsamples. Kinetic temperatures are found to be between 10 and 60 K and spatial densities in the range 10^5–10^6 cm^{-3}. Hotter, denser cores are found in a few HMPOs, indicating that these sources already harbour hot cores heated by protostars.

Key words. astrochemistry – ISM: molecules – ISM: clouds – molecular processes – stars: formation

1. Introduction

The last years have seen a major observational effort to compile samples of candidate high-mass protostellar objects (e.g., Molinari et al. 1996, 1998, 2000; Sridharan et al. 2002; Faúndez et al. 2004; Hill et al. 2005) and to study and understand the initial phases of evolution of high-mass stars (e.g., Hatchell et al. 2000; van der Tak et al. 2000b; Beuther et al. 2002a,b,c; Mueller et al. 2002; Hatchell & van der Tak 2003; Williams et al. 2004, 2005; De Buizer et al. 2005). The analysis of molecular spectra is a powerful diagnostic tool to investigate the properties of an interstellar cloud. Such spectra are fingerprints of a molecular cloud and they carry information on its chemistry, and therefore on its history, on its physical conditions, and on its dynamics and kinematics. Often, symmetric rotors such as NH_3, CH_3CN, and CH_3CCH are used to probe a cloud's kinetic temperature (Walmsley & Ungerechts 1983; Churchwell & Hollis 1983), while molecules with high dipole moment, e.g., CS, are used to determine its density (e.g., Snell et al. 1984; van der Tak et al. 2000b; Beuther et al. 2002a). However, different spatial distributions of the tracers (caused by their different chemistry) may complicate the picture, as they often probe physically different and spatially separate gas components (for chemical differentiation of NH_3 and CS, see, e.g.,Tafalla et al. 2002; for oxygen and nitrogen bearing molecules, Wyrowski et al. 1999). Chemical differentiation allows us to distinguish between the different physical components of a cloud and study them independently. However, when deriving physical parameters as density and temperature in a given region, it is desirable to make use of a single molecule: comparing results obtained by using different molecules may be misleading if the tracers do not co-exist.

Studies on slightly asymmetric rotors (H_2CO: Mundy et al. 1987; Mangum & Wootten 1993; CH_3OH: Leurini et al. 2004) reveal that these molecules can be used as diagnostic tools of both parameters, since such molecules allow determinations of density and often share a strong sensitivity to kinetic temperature with symmetric rotors. Leurini et al. (2004) discussed the tracing properties of CH_3OH, concluding that methanol is indeed a very useful tracer of physical conditions in star-forming regions, since it has a very rich spectrum of transitions spread throughout all of the centimetre, millimetre, and submillimetre spectral windows with energies above the ground state from zero to many hundreds of K. Moreover, it is ubiquitously found in different regimes of star formation, from quiescent, cold ($T \sim 10$ K), dark clouds (e.g., Friberg et al. 1988; Walmsley et al. 1988), to "hot core" sources near high-mass (proto)stellar objects (e.g., Menten et al. 1986, 1988) and it is associated with both dense cores and outflows of shocked gas (e.g., Bachiller et al. 1995).

Here we present methanol single-dish observations of a sample of sources in the early stages of high-mass star formation. In Sect. 2 the criteria used to select the sources are presented

⋆ Based on observations with the 100-m telescope of the MPIfR (Max-Planck-Institut für Radioastronomie) at Effelsberg, with the Caltech Submillimeter Observatory and with the IRAM 30 m telescope. IRAM is supported by INSU/CNRS (France), MPG (Germany), and IGN (Spain).

⋆⋆ Tables 7, 8 and Figs. 7 to 29 are only available in electronic form http://www.aanda.org

Table 1. The sample.

Source	RA [J2000]	Dec [J2000]	$v_{\rm lsr}$ [km s^{-1}]	d [kpc]
Infrared-dark clouds				
G11.11–0.12 P1	18 10 28.40	–19 22 29.0	29.0	3.6[a]
G19.30+0.07 P1	18 25 58.50	–12 03 59.0	26.0	2.2[a]
G28.34+0.06 P1	18 42 50.70	–04 03 16.0	78.0	4.8[a]
G33.71–0.01	18 52 59.10	+00 42 32.0	104.0	7.2[a]
G79.34+0.3 P1	20 32 21.80	+40 20 00.8	0.1	1.0[a]
High-mass (proto)stellar objects[b]				
I18089–1732–mm	18 11 51.5	–17 31 28.9	34.0	3.6[c]
I18151–1208–mm	18 17 58.0	–12 07 26.9	33.0	3.0[d]
I18182–1433–mm	18 21 09.2	–14 31 48.8	59.0	4.5[c]
I18264–1152–mm	18 29 14.6	–11 50 22.3	44.0	3.5[c]
I18310–0825–mm	18 33 47.9	–08 23 45.5	84.4	4.9[c]
I19410+2336–mm	19 43 10.9	+23 44 10.0	22.0	2.0[c]
I20126+4104–mm	20 14 25.9	+41 13 34.0	–4.0	1.7[e]
I23139+5939–mm	23 16 08.9	+59 55 12.9	–45.0	4.8[c]

[a] Carey et al. (1998). [b] The HMPO positions correspond to the dust continuum peaks observed by Beuther et al. (2002a). [c] Bontemps, priv. comm. [d] Sridharan et al. (2002). [e] Wilking et al. (1989).

and our centimetre, millimetre, and submillimetre observations discussed. In Sect. 3 we present the model used to analyse the CH_3OH data, while the results, together with a detailed description of each source, are discussed in Sect. 4.

2. Observations

2.1. Sample selection

The sources in our sample were selected from two databases of high-mass protostellar candidates, the infrared-dark clouds studied by Carey et al. (1998) and the high-mass protostellar objects from Sridharan et al. (2002), to cover a wide range of what are believed to be different evolutionary stages of massive star-forming cores. The infrared-dark cloud (hereafter IRDC) positions we observed stand out as (column density) peaks in the 850 μm dust emission (Carey et al. 2000). For many of these, further evidence (Pillai et al. 2006a) suggests them to be sites of active star formation. For the high-mass protostellar objects (hereafter HMPOs), we selected sources for which preliminary observations show strong CH_3OH emission (Sridharan et al. 2002). The sources of the sample are listed in Table 1. A detailed description of the two subsamples and of each individual source is given in Sect. 4.

2.2. Line selection

The main result of Leurini et al. (2004) is that CH_3OH transitions in the centimetre and millimetre spectrum are mainly density probes; however, when complete bands of lines with different energies and excitation ranges are observed, the information on the kinetic temperature can also be recovered. Since our sources are in different evolutionary stages and cover a wide range of physical conditions, from cold dense clouds in the IRDCs to more evolved sources, probably harbouring hot cores (some HMPOs), our observational data include bands of lines with a wide range of excitation conditions (~2–400 K). Simultaneously to the observations of the main isotopologue, $^{13}CH_3OH$ transitions were also observed to get more reliable estimates of optical depths. For our observations we selected:

- the $J_2 \rightarrow J_1$ band at 25 GHz, which is sensitive to the density;
- $J_0 \rightarrow J_{-1}$ band at 157 GHz, which traces density but, being a class II CH_3OH maser band, gives an insight into the IR radiation field;
- the $2_k \rightarrow 1_k$ band at 96.7 GHz, which is mainly tracer of densities higher than 10^5 cm^{-3} and has a weak dependence on temperatures up to 15–20 K;
- the $5_k \rightarrow 4_k$ band at 241.7 GHz, which mainly traces the density, but in the $k > 2$ lines is also sensitive to temperature;
- the $7_k \rightarrow 6_k$ band at 338 GHz, which is sensitive to both kinetic temperature and density;
- the $2_k \rightarrow 1_k$ $v_t = 1$ and the $5_k \rightarrow 4_k$ $v_t = 1$ bands at 96.5 and 241.2 GHz, which are sensitive to the radiation field and therefore to the temperature;
- the $2_k \rightarrow 1_k$, $J_0 \rightarrow J_{-1}$, and the $J_3 \rightarrow J_2$ $^{13}CH_3OH$ series at 94.4 GHz, 156 GHz, and 255 GHz, respectively.

Table 2. Spectral line observation parameters. Observatories are Effelsberg (Eff.), Pico Veleta (PV), and the Caltech Submillimter Observatory (CSO).

	Freq. [GHz]	*HPBW* [″]	Beam eff.	Telescope	Δv [km s^{-1}]
$J_2^0 - J_1^0$ $^{12}CH_3OH$	25	39[a]	0.52	Eff.	0.23
$2_k^1 - 1_k^1$ $^{12}CH_3OH$	96.5	26	0.78	PV	0.97
$2_k^0 - 1_k^0$ $^{12}CH_3OH$	96.7	26	0.78	PV	0.97
$J_0^0 - J_{-1}^0$ $^{12}CH_3OH$	157	16	0.69	PV	0.60
$5_k^1 - 4_k^1$ $^{12}CH_3OH$	241.2	10.4	0.52	PV	1.24
$5_k^0 - 4_k^0$ $^{12}CH_3OH$	241.7	10.4	0.52	PV	1.24
$7_k^0 - 6_k^0$ $^{12}CH_3OH$	338	21.4	0.75	CSO	0.62
$2_k^0 - 1_k^0$ $^{13}CH_3OH$	94.4	26.6	0.78	PV	0.99
$J_0^0 - J_{-1}^0$ $^{13}CH_3OH$	156	16	0.69	PV	1.20
$J_3^0 - J_2^0$ $^{13}CH_3OH$	255	9.9	0.46	PV	1.17

[a] At 1.3 cm the beam of the Effelsberg telescope is that of a 80 m telescope.

An overview of the observations is given in Tables 2 and 3. The pointing of the telescopes was checked often on several pointing sources; we consider our pointing accuracy to be within 5″ for the IRAM 30 m telescope and the Caltech Submillimeter Observatory, and 10″ for the Effelsberg 100 m telescope.

2.3. Effelsberg 100 m telescope

The $J_2 \rightarrow J_1$ E-band near 25 GHz was observed during winter 2001 and autumn 2002 with the MPIfR 100 m telescope near Effelsberg in frequency switching mode. Conversion factors from counts to antenna temperature are provided by the receiver group at different frequencies. Using the system temperature measurements, we determined the opacity during our observations and corrected for atmospheric absorption. Corrections for elevation are taken into account using the gain elevation curve [1]. The flux calibration was checked with continuum measurements of W3(OH) and NGC 7027 with an accuracy of 20%.

[1] `http://www.mpifr-bonn.mpg.de/div/ effelsberg/calibration/calib.html`

Table 3. Overview of the observations: + shows detections, – non-detections, and ? tentative detections. Empty space indicates non-observations. Observations of the $7^0_k - 6^0_k$ and $5^1_k - 4^1_k$ $^{12}CH_3OH$ bands (338 and 241 GHz) were performed for IRAS 18089–1732, together with the $2^0_k - 1^0_k$ and $J^0_0 - J^0_{-1}$ $^{13}CH_3OH$ bands (94.4 and 156 GHz).

	$^{12}CH_3OH$					$^{13}CH_3OH$
Source	$J^0_2 - J^0_1$ 25 GHz	$2^1_k - 1^1_k$ 96.5 GHz	$2^0_k - 1^0_k$ 96.7 GHz	$J^0_0 - J^0_{-1}$ 157 GHz	$5^0_k - 4^0_k$ 241.7 GHz	$J^0_3 - J^0_2$ 255 GHz
G11.11–0.12 P1		–	+	+	+	–
G19.30+0.07 P1	+	–	+	+	+	–
G28.34+0.06 P1	–	–	+	+	+	–
G33.71–0.01	–	–	+	+	+	–
G79.3+0.3 P1		–	+	+	+	–
18089–1732	+	+	+	+	+	+
18151–1208	+	–	+	+	+	–
18182–1433	+	?	+	+	+	+
18264–1152	+	–	+	+	+	–
18310–0825		–	+	+	+	–
19410+2336	+	–	+	+	+	–
20126+4104	–	–	+	+	+	–
23139+5939	–	–	+	+	+	–

2.4. IRAM 30 m telescope

The IRAM 30 m telescope was used in August 2002 and January 2003 to observe our sample at 96 GHz, 157 GHz, and 241 GHz in the $2_k \rightarrow 1_k$, $J_0 \rightarrow J_{-1}$, and $5_k \rightarrow 4_k$ CH_3OH series. This setup also allows the simultaneous observation of the $2_{k,v_t=1} \rightarrow 1_{k,v_t=1}$ at 96.5 GHz and of the $5_{-1,v_t=1} \rightarrow 4_{-1,v_t=1}$-*A* line at 241.4 GHz. Nine-point maps with a spacing of 6″ were performed toward each source to cover the 3 mm beam of the telescope with the 2 mm and 1 mm beams. The observations were done in the wobbler switching mode, with a throw in azimuth by 240″ between the ON and OFF positions. To have a reliable estimate of the optical depth, the $J_3 \rightarrow J_2$ $^{13}CH_3OH$ series at 255 GHz was also observed. For IRAS 18089–1732, additional data in the $5_k \rightarrow 4_k$ CH_3OH series in the first torsionally excited state were taken with the same observing strategy as for the ground state lines, simultaneously to the $2_k \rightarrow 1_k$, $J_0 \rightarrow J_{-1}$ $^{13}CH_3OH$ series, at 94.4 GHz and 156 GHz, respectively. For the analysis of the IRAM data, the spectra were convolved to the spatial resolution of the 3 mm spectra; in this way the same emitting region is analysed when modelling the different bands simultaneously (see Sect. 3).

2.5. Caltech Submillimeter Observatory (CSO)

In May 2004, the CSO 10.4 m telescope on Mauna Kea, Hawaii, was used to observe the $7_k \rightarrow 6_k$ CH_3OH series at 338 GHz. However, due to very poor weather conditions, only observations toward one of the sources, IRAS 18089–1732, were performed. The observations were done in the wobbler switching mode, with the wobbler switching in azimuth by 180″ between the ON and OFF positions. Flux calibration was obtained by observing Uranus.

3. CH_3OH analysis

Leurini et al. (2004) investigated the diagnostic properties of CH_3OH over a range of physical parameters typical of high-mass star-forming regions. However, the energy level dataset they used is incomplete for energies above 100 K and does not ensure reliable results for warm/hot sources. Here, we extend the calculations to a dataset better suited for more evolved sources, as some HMPOs in our sample do definitely contain hot cores, as suggested by the detection of typical hot core molecules (CH_3OCH_3 and $HCOOCH_3$, Leurini & Schilke 2007). Our new analysis includes all the levels up to ($J = 14$, $k = 13$) in the torsional ground state and up to $(J, k) = 9$ in the first torsionally excited state. Levels from the second torsionally excited state (with typical energies of ∼500 K above the ground state) are not included in the calculations because of the lack of available rates. Models of methanol class II masers (e.g., Sobolev & Deguchi 1994; Cragg et al. 2005) show that levels from the first two torsionally excited states are essential to the pumping of these masers. We cannot estimate the errors in the calculation of the non-inverted level populations due to neglecting the $v_t = 2$ levels. However, given the typical energies of the $v_t = 2$ levels and the evolutionary phase of our sources, we assume that the influence of the $v_t = 2$ levels on the thermal lines in the ground state is negligible in our sample of sources. The new level dataset is shown in Fig. 1. Energies are calculated using global fit parameters reported in Xu & Hougen (1995).

Radiative transitions within the $v_t = 1$ state are included as well as transitions between the $v_t = 1$ and the ground state, with Einstein coefficients derived by Mekhtiev et al. (1999). Collisional rates for $(J, k) > 9$, $v_t = 0$, were extrapolated from the results of Pottage et al. (2002), using the propensity rules derived from the $(J, k) \leq 9$ rates. Collisional rate coefficients for CH_3OH-*A* and -*E* species in the $v_t = 1$ state with He were recently computed by Pottage et al. (2004) at 20 K. They found the cross sections for the torsionally inelastic transitions ($\Delta v_t \pm 1$) to be typically two orders of magnitude smaller than for torsionally elastic transitions ($\Delta v_t = 0$) and characterised by no propensity rules. We scaled their results for torsionally elastic collisions to higher temperatures by a factor $(T/20)^{1/2}$ (Flower, priv. comm.), and assumed the torsionally inelastic collisional rates to be two orders of magnitude smaller than the rotationally inelastic transitions within the $v_t = 0$ state.

For IRAS 18089–1732 and IRAS 18182–1433, where we detected $^{13}CH_3OH$, the $^{13}CH_3OH$ data were included in the analysis. We used line strengths and rest frequencies from the Cologne Database for Molecular Spectroscopy (Müller et al. 2001)[2], which includes the measurements by Xu & Lovas (1997). We used a level dataset up to $(J, k) = 9$ in the calculations, that has an incomplete coverage in energy above 100 K (see Fig. 2). This

[2] http://www.cdms.de

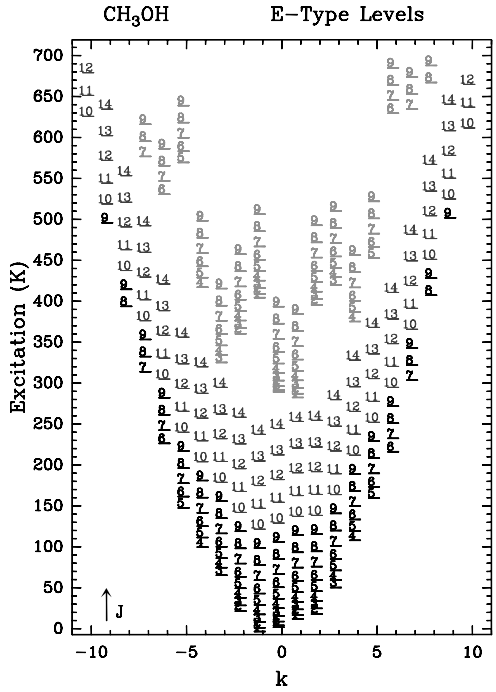

Fig. 1. Energy levels for the E−symmetry state of CH_3OH with an energy above the ground state of less than 700 K: in black, levels for which CH_3OH-He collisional rates were computed by Pottage et al. (2002) for the $v_t = 0$; in dark grey, levels for which CH_3OH-He collisional rates were extrapolated; in light grey, $v_t = 1$ levels for which collisional rates were computed by Pottage et al. (2004) at 20 K and which were then extrapolated at higher temperatures.

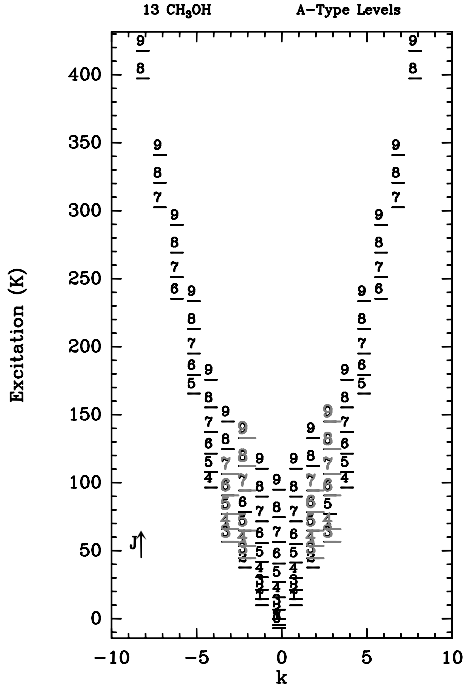

Fig. 2. Partial energy level diagram for $^{13}CH_3OH$-*A*. The levels involved in the observed transitions are marked in grey.

may result in erroneous level populations for $^{13}CH_3OH$ at high temperatures. Since collisional rate coefficients are not available for $^{13}CH_3OH$ we used the coefficients for $^{12}CH_3OH$. The abundance of $^{13}CH_3OH$ relative to $^{12}CH_3OH$ was estimated using the relation between the isotopic ratio $^{12}C/^{13}C$ and the distance from the Galactic centre (D_{GC}) (Wilson & Rood 1994):

$$^{12}C/^{13}C = (7.5 \pm 1.9)\, D_{GC}[\mathrm{kpc}] + (7.6 \pm 12.9) \quad (1)$$

with D_{GC} = 5.1 and 4.4 kpc for IRAS 18089–1732 and IRAS 18182–1433 (Beuther priv. comm.).

3.1. Infrared pumping

Leurini et al. (2004) did not include any external radiation fields other than the cosmic microwave background in their analysis. Therefore, they neglected any effect due to infrared pumping. When zooming into the inner regions of a cloud, close to the central massive protostars, infrared radiation fields are not negligible and competition between collisions and the IR radiation field in the excitation of the energy levels is a known phenomenon (for CS see Carroll & Goldsmith 1981; Hauschildt et al. 1993).

In Fig. 3a (and Fig. 7), the effect of IR pumping on the excitation of CH_3OH is illustrated; for the torsional ground-state lines it is virtually impossible to distinguish between IR pumping and pumping by collisions. However, a promising way to break the degeneracy is by observations of vibrationally or torsionally excited lines, as, with very high critical densities (10^{10}–10^{11} cm^{-3}) and high level energies ($T \geq 200$ K), they are hardly populated by collisions (Figs. 3b and 7), but trace the IR field instead. Therefore, for hot sources, reliable determinations of density and kinetic temperature are possible only when observations of $v_t = 1$ bands are available.

3.2. The model

The large velocity gradient (LVG) method assuming spherical geometry, in the derivation of de Jong et al. (1975), was used for solving the radiative transfer equations. Since the only IR radiation relevant for the excitation of the methanol transitions we observed arises in the range 28–45 μm, exciting the $v_t = 1$ level, we cannot derive the spectral energy distribution. What counts is the number of photons at these wavelengths, which we parametrise as follows:

$$J_{\mathrm{ext}} = w \times J(T_{\mathrm{d}}) \times (1 - \mathrm{e}^{-\tau_{\mathrm{d}_\nu}}) \quad (2)$$

$$\tau_{\mathrm{d}_\nu} = \tau_{\mathrm{d}_0} \times \left(\frac{\nu}{\nu_0}\right)^{\beta}, \quad (3)$$

where $J(T_{\mathrm{d}}) = [\exp(h\nu/kT_{\mathrm{d}}) - 1]^{-1}$ and w is a dilution factor. The optical depth of the dust, τ_{d}, is given by a power law of the frequency; τ_{d_0} is the reference optical depth of the dust at 100 μm. The values of β and of τ_{d_0} are taken from the literature.

Models of masers transitions from different molecular species showed that deviation from thermal equilibrium between gas and dust may have important effects on the calculations (e.g., Cesaroni & Walmsley 1991; Sobolev & Deguchi 1994). However, we do not have enough observations to constrain the dust temperature, and, following Krügel & Walmsley (1984), we assume that the gas and the dust are thermally coupled at high density ($n_{\mathrm{H_2}} > 10^5$ cm^{-3}), $T_{\mathrm{d}} = T_{\mathrm{gas}}$. In this way, all the parameters in Eq. (2) are fixed.

Since the information we have is not enough to constrain w, we used the detection of torsionally excited lines to turn on ($w = 1$ in Eq. (2)) the dust radiation field in the calculations. The torsionally excited lines are clearly detected only in IRAS 18089-1732, and tentatively in IRAS 18182-1433, where the signal-to-noise ratio is one in the $2^1_k \rightarrow 1^1_k$ lines and three in the $5^1_{-1} \rightarrow 4^1_{-1}$-*A* transition. The integrated intensities of these

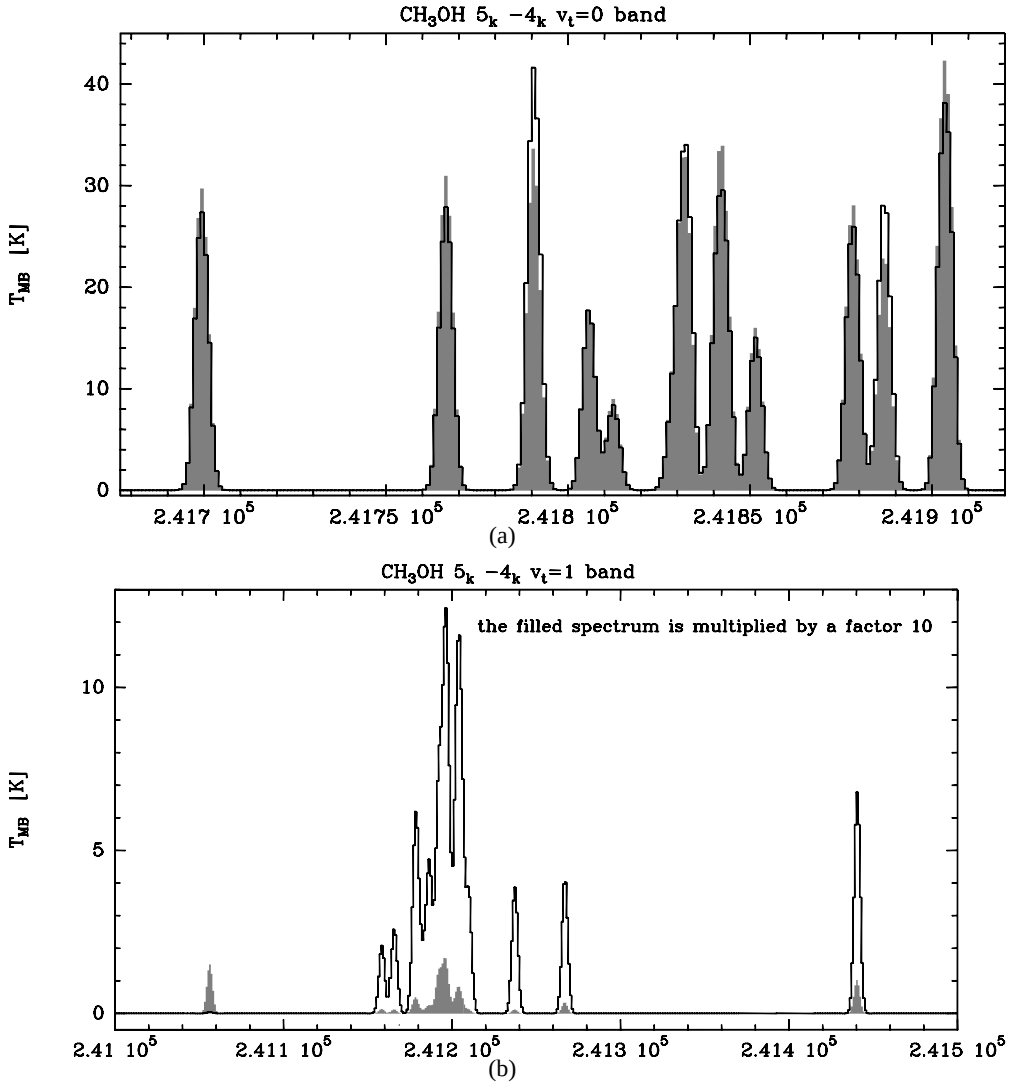

Fig. 3. a) (*Top*) and **b)** (*bottom*) illustrate how excitation by IR vibrational pumping mimics the effect of collisions in populating the $v_t = 0$ CH_3OH levels. In grey, synthetic spectra are shown for which pure collisional pumping ($n(H_2) = 10^8$ cm^{-3}, $N_{CH_3OH-E} = N_{CH_3OH-A} = 10^{17}$ cm^{-2}, no radiation field) is populating the $v_t = 0$ levels **a**) and the $v_t = 1$ levels **b**); the black line shows the synthetic spectra for the same levels when only the IR radiation field is pumping the system, ($n(H_2) = 10^3$ cm^{-3}, radiation field given by a grey-body at $T_d = 190$ K). The synthetic spectra are computed with a source size of 1″, a resolution that can be reached by an interferometer with a baseline of 300 m. While the ground-state spectra are virtually indistinguishable, the $v_t = 1$ spectra show how inefficiently the pure collisional pumping excites the torsionally excited levels. The synthetic spectrum for the $v_t = 1$ band shows very low line intensities (multiplied by a factor of 10 in the plot) when pure collisional pumping is used. Similar results are presented for other bands as on-line material (Fig. 7).

transitions are reported in Table 8. The dust radiation field is used only for the level populations of the hottest component of these sources. In all other sources, no dust radiation field is used ($w = 0$).

This treatment was chosen for reasons of simplicity, as the dust radiation field is not constrained enough to warrant any more sophisticated modelling (e.g., Deguchi 1981) that takes into account absorption of line photons by the dust. We are aware that the treatment of the IR field is quite simplistic; however it is probably not more inaccurate than the treatment of the gas consisting of components of homogeneous temperature and density (see Sect. 3.3). Still, we feel that we are able to determine the essential features of the sources. A model trying to explain the observations of the various stages using a realistic source structure and a better treatment of the radiation field is highly desirable, and we plan to take this step in the future.

3.3. Analysis technique

The fitting procedure used to analyse the data is described by Leurini et al. (2004) and it is based on the simultaneous fit of all the measured lines with a synthetic spectrum computed using the model in Sect. 3.2. The best fit is then obtained by minimizing the χ^2 between the data and the model spectrum with the Levenberg-Marquardt method (Press et al. 1992). All channels where methanol can emit are included in the fit, even if the transitions are not detected. For the sake of simplicity, we make the assumption that the source can be reasonably well approximated by a small number of non-interacting components, i.e., the line intensities add up taking into account local line overlap from the different components (see Eq. (13) in Cesaroni & Walmsley 1991; and Eq. (3) in Leurini et al. 2004). No density or temperature profiles are used, but each component is represented by a spherical cloud of uniform physical conditions. However, these

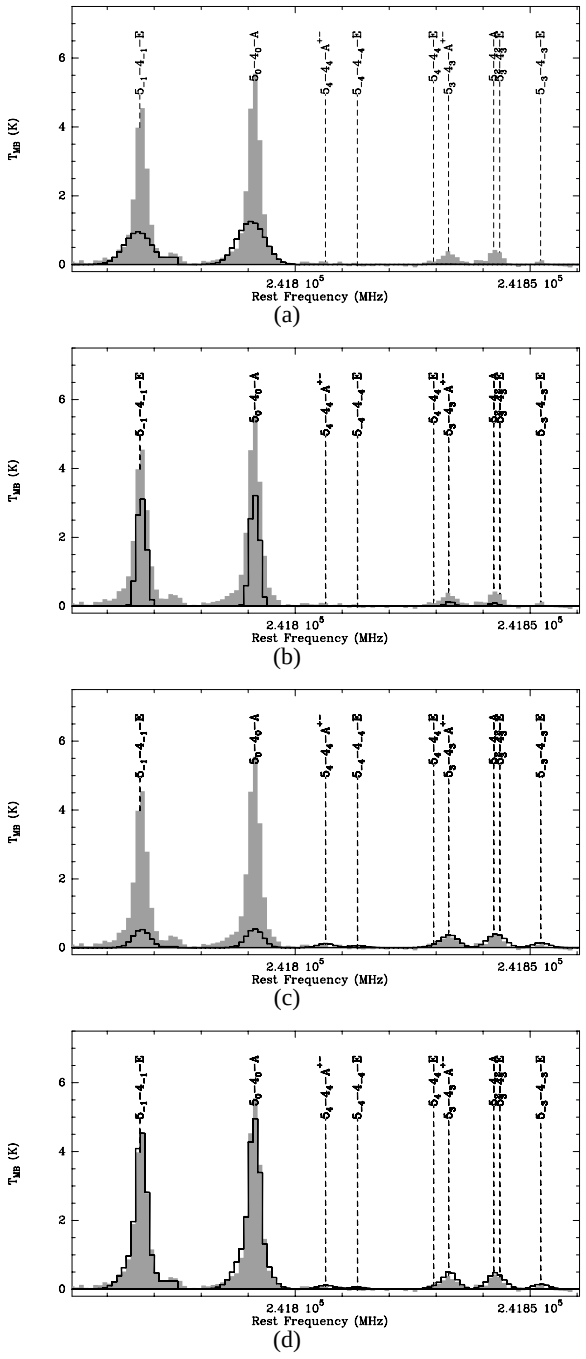

Fig. 4. In grey, the observed spectrum towards IRAS 18264–1152 at 1 mm (**a), b), c), d)**) is shown; overlaid in black, the contribution to the total emission from component 1 **a)** , 2 **b)**, component 3 **c)** of Table 4, and their sum **d)**.

different components most likely represent nested layers of the density and temperature source structure, rather than spatially distinct regions. In Fig. 4 the contribution of each component to the total emission is shown for the 1 mm band, for IRAS 18264–1152.

A more detailed model of the sources, including density and temperature distributions, would be desirable (for a compilation of different methods, see van Zadelhoff et al. 2002). On the other hand, little detailed information on the sources of our sample exists and almost no high (i.e., arcsec) resolution data are available. Therefore any assumption on the morphology would be poorly constrained. While a more detailed model would be better suited to the analysis of a single source, it would be extremely time-consuming and prohibitive for a large sample of sources. Our technique allows investigation of the parameter space, checking whether the found solution is global or local. It also allows error estimates for the derived parameters (see discussion in Sect. 3.5), while most published studies (Monte Carlo, Accelerated Lambda Iteration) employ a trial and error comparison of the fits to data.

The free parameters in the fit are the kinetic temperature, the density of the gas, and the CH_3OH-*E* and -*A* column densities. Linewidths and velocities are given as input and are fixed parameters in the fit. They are derived by fitting a Gaussian profile to the transitions not blended with other lines. Because of the degeneracies with column density (in the optically thin case) or temperature (in the optically thick case) no formal fitting of the source size was performed. The sizes were determined either by direct interferometric and dust continuum measurements, or by our own data.

For the warmest sources of the sample, lines are expected to be optically thick, at least in the lower excitation transitions. By fitting optically thick lines, the derived physical parameters are the ones at the surface where the gas becomes opaque, while optically thin lines reflect the conditions in an inner region in the source. When $^{13}CH_3OH$ and/or $^{12}CH_3OH$ $v_t = 1$ lines are observed, results obtained by fitting these transitions are more relevant to the source interiors than results derived from the analysis of optically thick lines alone.

3.4. Maser activity

Although in several sources of our sample class I and/or class II masers are detected, these transitions are not included in the following χ^2 analysis. The model predictions for these lines are shown in Figs. 9–29 for comparisons with the observations. To properly model the maser intensities, beaming and the amplification of background photons have to be taken into account. Therefore, our analysis is not tailored for explaining CH_3OH maser data, which have been intensively studied by other authors (e.g., Sobolev & Deguchi 1994; Sobolev et al. 1997; Cragg et al. 2005), and we refer to these studies for an analysis of the physical properties of maser spots.

3.5. Errors of the fitted parameters

To investigate whether the solution is local or global and to estimate the uncertainty of each fitted parameter, an analysis of the χ^2 distribution as function of the different free parameters is desirable. This implies working in a $\Sigma_c N_c$-D space, where the sum is over the components and N_c is the number of free parameters of component *c*. For most of our sources, the variation of one parameter in one component could be compensated by changing another, as column density, temperature, and source size are correlated. Investigating the distribution of the χ^2 around the minimum, for dependent parameters, is achieved by varying each parameter in an interval that is reasonably close to the minimum and re-optimizing the remaining free parameters. This results in a very time-consuming procedure when done on such a large number of sources and has the additional problem of visualising the results, since, for models with three components, this requires working in a 12-D hypercube.

Another way to estimate the uncertainty on the fitted parameters, accounting for the noise in the spectra, is the Monte Carlo

error analysis (Lampton et al. 1976), where the fitting method is run over synthetic spectra obtained by adding a random Gaussian noise of standard deviation equal to the original data error to the best-fit spectrum and repeating for a high number of interactions. The uncertainty on the fitted parameters were computed by using the Monte Carlo error analysis, as this method is the only manageable one in terms of computing time. The results are listed in Table 5.

All transitions are included in the analysis, even in case of non detection. All channels within $4 \times \Delta v$ km s^{-1} from the rest frequency of each transition are included in this analysis. This is an arbitrary number, but, since emission at the edge of this range is lost in the noise, it may affect our results only by overestimating the uncertainties in the parameters. Uncertainties in the source sizes and in the velocities are not taken into account.

For two sources of the sample, IRAS 18089–1732 and IRAS 18264–1152, we are not able to derive errors for the parameters using the Monte Carlo method, as the computing time is prohibitive due to the high number of observed transitions. However, in Fig. 5 we show cuts in the χ^2 along the $[T, n]$, $[T, N]$, and $[n, N]$ planes for the outer component in IRAS 18089–1732 (component 1 in Table 4), obtained by keeping fixed all the other parameters to the value in Table 4. No meaningful constraints for the parameters can be derived from this analysis, as the true confidence regions in a plane should be computed by projecting the N-dimensional regions in the plane of interest. However, these figures show that the χ^2 distribution is, at least in these planes, a well-behaved function, with only one minimum. The same plots, for the other two components, are shown in the on-line material (Fig. 8). For the other two components, the gas is thermalised and no upper limits to the density are derived (Figs. 8a,d).

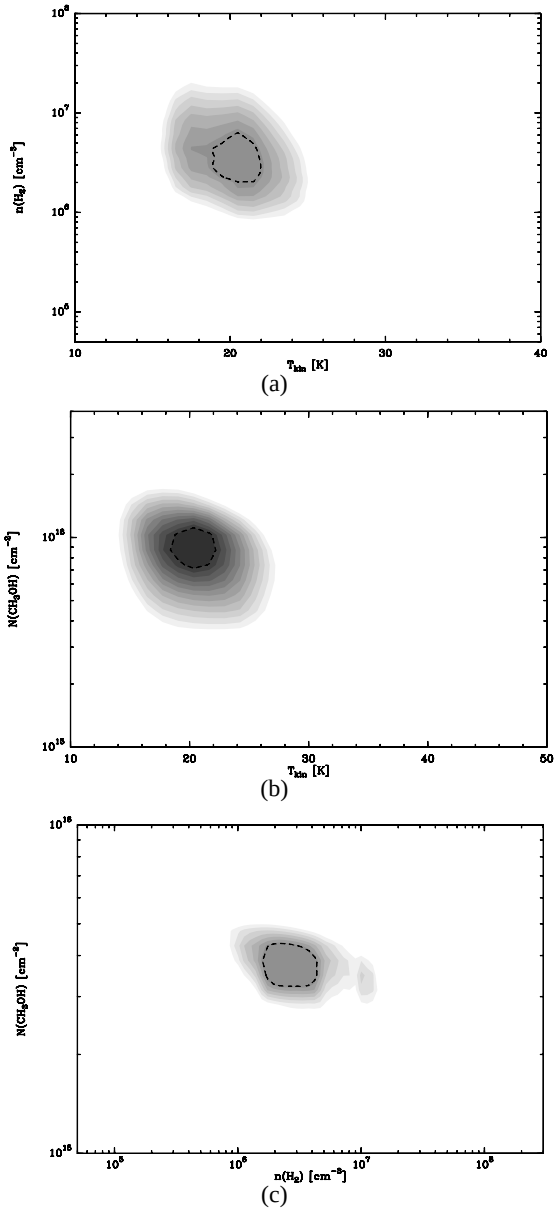

Fig. 5. The χ^2 distribution for IRAS 18089–1732 in the $[T, n]$ **a)**, $[T, N]$ **b)**, $[n, N]$ **c)**, planes for the component 1 in Table 4, with all other parameters fixed to the parameters given in Table 4. The 3σ confidence region lies between the dashed contours.

4. Model results

In the following sections, our model results are discussed within the context of the known properties of each source. In Table 4 the derived physical parameters are listed. CH_3OH abundances are given for each component as a sum of the two symmetry states, A and E; H_2 column densities are derived from the densities obtained with the LVG analysis, assuming spherical geometries. In Table 5, the 3σ range for our estimates of T_K, $n(H_2)$, $N(CH_3OH$-$A)$, and $N(CH_3OH$-$E)$ are given. The synthetic spectra overlaid on the data are shown in Figs. 9–29.

4.1. Infrared-dark clouds

The IRDCs are a population of several thousand molecular clouds that were identified by their mid-infrared extinction in ISOGAL (Perault et al. 1996) and MSX (Midcourse Space Experiment) images (Egan et al. 1998). Egan et al. (1998) concluded that IRDCs have visual extinctions higher than hundred magnitudes indicating very large column densities of cold dust. Centimetre- and (sub)millimetre line observations reveal typical temperatures of $T \leq 20$ K and densities $n(H_2) \geq 10^5$ cm^{-3} (Carey et al. 2000; Pillai et al. 2006a). Submillimetre continuum observations suggest that high-mass star formation may be occurring in some regions within IRDCs (Carey et al. 2000). Based on their NH_3 (1, 1) and (2, 2) observations and given the existence of methanol masers, Pillai et al. (2006a) come to the same conclusion. Moreover, some sources exhibit non-Gaussian line profiles in several molecular species (H_2CO, see Carey et al. 1998; HCO^+, see Redman et al. 2003), which could be explained by infall (Redman et al. 2003) or (in the cases of wide wings) outflows. In the following discussion, we refer to the positions we observed, which correspond to the submillimetre emission peaks detected by Carey et al. (2000), as IRDCs.

4.1.1. G11.11–0.12 P1

G11.11–0.12 is a filamentary cloud, as revealed by the 8 μm MSX extinction map by Carey et al. (1998), continuum observations at 850 μm (Carey et al. 2000), and NH_3 maps (Pillai et al. 2006a) From the analysis of the submillimetre continuum, Carey et al. (2000) derive a dust temperature of the brightest submillimetre peak ranging between 25 and 43 K, depending on the spectral index used for modelling the dust emissivity, and a total mass between 67 and 150 $M_\odot$. Detection of the NH_3 (3, 3) transition reveals a higher temperature component (Pillai et al. 2006b). Recently, Pillai et al. (2006b) reported the discovery of maser action in the $5_1 \rightarrow 6_0$-A^+ CH_3OH transition at 6.7 GHz

Table 4. CH_3OH model results. In Col. 1, out refers to "outflow", ex to "extended", and core to the "inner" component.

	Δv (km s^{-1})	$v_{\rm lsr}$ (km s^{-1})	$T_{\rm K}$ (K)	$n(H_2)$ (cm^{-3})	$N(CH_3OH\text{-}A)$ (cm^{-2})	$N(CH_3OH\text{-}E)$ (cm^{-2})	Source size ($''$)	$[CH_3OH]/[H_2]$	$\chi^2_{\nu_{\rm d}}$
G11.11–0.12 P1									2.2
1 comp. (ex)	4.	30.0	18.0	1×10^5	2×10^{14}	3×10^{14}	22[a]	4×10^{-9}	
2 comp. (core)	4.7	29.8	47.0	1.7×10^6	1.2×10^{16}	9.6×10^{15}	2.0	1×10^{-7}	
G19.30+0.07 P1									2.1
1 comp. (out)	15.0	23.8	11	1×10^5	2.7×10^{15}	2.7×10^{15}	12.5	1×10^{-7}	
2 comp. (core)	4.5	26.7	59.3	2.5×10^5	1×10^{16}	1×10^{16}	6.0	7×10^{-7}	
G28.34+0.06 P1									4.9
1 comp. (ex)	2	79.0	29	6×10^4	2.4×10^{14}	2.2×10^{14}	19	6×10^{-9}	
2 comp.(out)	9	80.8	23	3.5×10^4	1.5×10^{15}	1.5×10^{15}	13	9×10^{-8}	
3 comp. (core)	3.6	79.9	35	6×10^5	1.5×10^{15}	1.5×10^{15}	8	9×10^{-9}	
G33.71–0.01									4.8
1 comp. (out)	7.0	105.5	12.4	5.5×10^4	5.3×10^{14}	5.3×10^{14}	19	9×10^{-9}	
2 comp. (ex)	4.0	105.5	33	7.7×10^5	1.2×10^{15}	8.2×10^{14}	11	2×10^{-9}	
G79.34+0.3 P1									1.4
1 comp. (ex)	2.0	0.5	17.2	$2.\times10^5$	7.8×10^{13}	7.6×10^{13}	32.0	1×10^{-9}	
18089–1732									2.2
1 comp. (ex)	4.0	32.9	21.8	2.8×10^6	4.3×10^{15}	3.7×10^{15}	8.5	6×10^{-9}	
2 comp. (core)	3.1	32.7	45	7.0×10^7	4.1×10^{17}	3.1×10^{17}	1.7[a]	1×10^{-7}	
3 comp. (core)	4.6	32.7	300	1.0×10^8	9.0×10^{17}	9.0×10^{17}	0.5[a]	5×10^{-7}	
18151–1208									1.9
1 comp.(ex)	3.5	34.3	29	2.4×10^6	2.8×10^{14}	2.5×10^{14}	20.0	2×10^{-10}	
18182–1433									1.7
1 comp. (out)	9.0	60.1	18	3.5×10^5	2.7×10^{14}	2.7×10^{14}	24	1×10^{-9}	
2 comp. (ex)	2.8	60.1	28.7	1.4×10^6	8×10^{14}	8×10^{14}	13.4[b]	1×10^{-9}	
3 comp. (core)	4.7	59.9	62.3	4.3×10^6	6.8×10^{16}	6.8×10^{16}	3.0	2×10^{-7}	
18264–1152									2.3
1 comp. (out)	8.0	44.6	23	2.9×10^5	9.9×10^{14}	8×10^{14}	17[b]	7×10^{-9}	
2 comp. (ex)	2.5	43.7	50	6.5×10^5	3.2×10^{15}	3.2×10^{15}	9	2×10^{-8}	
3 comp. (core)	5.0	43.7	90	2.5×10^6	1.3×10^{16}	1.3×10^{16}	4[a]	5×10^{-8}	
18310–0825									2.0
1 comp. (ex)	2.4	84.2	16.6	1.8×10^5	2.7×10^{14}	2.2×10^{14}	18.5	2×10^{-9}	
19410+2336									3.4
1 comp. (ex)	3.0	22.9	18.6	1.7×10^5	4.6×10^{14}	4.0×10^{14}	20.0[c]	9×10^{-9}	
2 comp. (core)	3.0	22.0	52.8	5.0×10^6	4.7×10^{15}	4.7×10^{15}	5.0	1×10^{-8}	
20126+4104									1.4
1 comp. (ex)	4.4	–2.6	36.4	1.7×10^6	2.5×10^{14}	2.4×10^{14}	15.0[c]	7×10^{-10}	
2 comp. (core)	6.0	–3.0	77.8	1.9×10^7	2.0×10^{17}	1.9×10^{17}	1.2[c]	6×10^{-7}	
23139+5939									2.7
1 comp. (out)	9.0	–44.7	16	1×10^5	2.5×10^{14}	2.8×10^{14}	19.5[b]	2×10^{-9}	
2 comp. (ex)	4.0	–46.2	30	7.7×10^5	2.4×10^{15}	2.2×10^{15}	8	2×10^{-8}	

[a] Wyrowski, unpublished data. [b] Based on (Beuther et al. 2002a), adjusted to fit the data. [c] Cesaroni et al. (1997) identified an extended region of 15″ and detected a hot core of source size less than 1.3″.

toward the dust submm continuum peak. Our CH_3OH observations show non-Gaussian profiles in the $2_k \rightarrow 1_k$ and $5_k \rightarrow 4_k$ $k = 0, -1$ lines. A two component model was used to fit the data, one component for the wings emission and one for the core. The first component has a size of 22″ and "average" IRDC properties, with regard to $T_{\rm K}$ and n. The second one, of 2″ size, is warmer and denser. These results are in agreement with the NH_3 analysis from Pillai et al. (2006b), who fitted the single dish NH_3 spectrum with two components, one with source size 23″ and $T_{\rm kin}$ = 15.4 K, the other with s = 3.3″ and $T_{\rm kin}$ = 60 K. The methanol abundance is enhanced in the compact, hotter component by two orders of magnitude over typical dark cloud conditions ($X_{\rm CH_3OH} \sim 10^{-10}$–$10^{-9}$ Friberg et al. 1988; Walmsley et al. 1988). For this second component, we find a temperature and density below typical class II CH_3OH maser conditions. However, analysing our nine point map of the source, the emission peak is offset from the central position, which suggests we are missing the denser, hotter component from which the maser emission arises. Alternatively, a hotter component with a small size could be not detectable due to beam dilution.

4.1.2. G19.30+0.07 P1

The analysis of the submillimetre continuum emission at G19.30+0.07 P1 leads to dust temperatures between 14 and 25 K and masses in the range 33–93 $M_\odot$; estimates of gas temperature and density were done by Pillai et al. (2006a) from NH_3 data and by Leurini et al. (2004) from CH_3OH. The former found a kinetic temperature of 18.5 K, which is probably a lower limit as only the (1, 1) and (2, 2) lines were analysed. The previous calibration of the 2 mm and 1 mm spectra presented by Leurini et al. (2004) was not correct. Our new analysis of the re-calibrated data is performed with two components, one for the non-Gaussian wings, the other for the main emission. In our previous analysis, the red wing of the $5_{-1} \rightarrow 4_{-1}$-$E$ line was not included, as emission in the HNCO $11_{0,11} - 10_{0,10}$ transition could

Table 5. CH_3OH model results: 3σ range. In Col. 1, out refers to "outflow", ex to "extended", and core to the "inner" component.

Source	T_K (K)	$n(H_2)$ (cm^{-3})	$N(CH_3OH\text{-}A)$ (cm^{-2})	$N(CH_3OH\text{-}E)$ (cm^{-2})
G11.11–0.12				
1 comp.(ex)	16–19	6×10^4–1×10^5	8×10^{13}–6×10^{14}	1×10^{14}–$\times10^{15}$
2 comp.(core)	38–54	1×10^6–2×10^6	9.8×10^{15}–1.5×10^{16}	8.0×10^{15}–1.1×10^{16}
G19.30+0.07 P1				
1 comp.(out)	7–13	6.9×10^4–1.2×10^5	2.4×10^{15}–2.8×10^{15}	2.4×10^{15}–2.7×10^{15}
2 comp.(core)	55–63	1.1×10^5–3.6×10^5	9.4×10^{15}–1.0×10^{16}	9.6×10^{16}–1.0×10^{16}
G28.34+0.06				
1 comp.(ex)	26–31	3×10^4–7×10^4	1.9×10^{14}–2.6×10^{14}	1.5×10^{14}–2.5×10^{14}
2 comp.(ex)	21–25	2×10^4–5.0×10^4	1.3×10^{15}–1.5×10^{15}	1.3×10^{15}–1.5×10^{15}
3 comp.(core)	33–40	5×10^5–7×10^5	1.3×10^{15}–1.5×10^{15}	1.3×10^{15}–2.6×10^{15}
G33.71–0.01				
1 comp.(out)	11–13	3.1×10^4–6.3×10^4	4.2×10^{14}–5.4×10^{14}	4.1×10^{14}–5.2×10^{14}
2 comp.(ex)	29–36	6.0×10^5–8.2×10^5	1.0×10^{15}–1.2×10^{15}	7.0×10^{14}–8.5×10^{14}
G79.34+0.3 P1				
1 comp.(ex)	16–19	1.5×10^5–2.1×10^5	9.8×10^{13}–1.5×10^{14}	9.4×10^{13}–1.4×10^{14}
18151–1208				
1 comp.(ex)	24–33	1.9×10^6–2.7×10^6	2.0×10^{14}–2.8×10^{14}	1.9×10^{14}–2.6×10^{14}
18182–1433				
1 comp.(out)	15–22	2.6×10^5–4×10^5	2×10^{14}–3×10^{14}	2×10^{14}–3×10^{14}
2 comp.(ex)	26–32	1×10^6–2×10^6	6.7×10^{14}–9×10^{14}	7×10^{14}–9×10^{14}
3 comp.(core)	58–63	4×10^6–5×10^6	6×10^{16}–7×10^{16}	6×10^{16}–7×10^{16}
18310–0825				
1 comp.(ex)	13–20	1.3×10^5–2.1×10^5	1.9×10^{14}–3.4×10^{14}	1.6×10^{14}–3×10^{14}
19410+2336				
1 comp.(ex)	13–20	1.2×10^5–2.2×10^5	3.4×10^{14}–4.9×10^{14}	2.8×10^{14}–4.2×10^{14}
2 comp.(core)	39–53	4.3×10^6–5.1×10^6	4.6×10^{15}–5.4×10^{15}	4.6×10^{15}–5.4×10^{15}
20126+4104				
1 comp.(ex)	29–42	1×10^6–2×10^6	1.7×10^{14}–2.6×10^{14}	1.6×10^{14}–2.6×10^{14}
2 comp.(core)	74–81	1×10^7–2×10^7	1.8×10^{17}–2.1×10^{17}	1.7×10^{17}–2×10^{17}
23139+5939				
1 comp.(out)	13–18	6.5×10^5–1.1×10^5	1.8×10^{14}–2.8×10^{14}	1.8×10^{14}–2.7×10^{14}
2 comp.(ex)	27–33	6.5×10^5–7.8×10^5	2.1×10^{15}–2.5×10^{15}	1.9×10^{15}–2.2×10^{15}

blend with the CH_3OH profile. However, similar non-Gaussian profiles are found in all the $k = 0, -1$ lines, at 3 mm and 2 mm. We believe that it is more reasonable to assign the 1 mm profiles to a broader component with a width of 15 km s^{-1}, shifted in velocity by –2.5 km s^{-1} with respect to the main emission, rather than invoking the presence of HNCO emission. The first component has typical physical conditions for IRDCs, while the kinetic temperature derived for the second one is higher than expected for this population of sources. The methanol abundance relative to H_2 is in both cases higher than typical dark cloud values.

4.1.3. G28.34+0.06 P1

G28.34+0.06 P1 is one of the three dust subcores in the IRDC G28.34+0.06. It has a kinetic temperature of ∼16.6 K as derived from the NH_3 (1, 1) and (2, 2) inversion lines (Pillai et al. 2006a). The submillimetre continuum data lead to a dust temperature between 17 and 34 K, depending on the spectral index used for modelling the dust emissivity, and a total mass between 120 and 400 $M_\odot$ (Carey et al. 2000). Methanol emission is strong in all the millimetre bands observed, but highly excited lines are not detected. Non-Gaussian wings are detected in the $5_{-1} \rightarrow 4_{-1}$-*E* and $5_0 \rightarrow 4_0$-*A* at 1 mm. We model the source with three components. The first, cold, extended, and not very dense, is mainly responsible for the Gaussian emission at 3 mm; the second one produces the emission in the wings, the third the bulk emission. The derived temperatures are higher than what inferred from NH_3 (1, 1) and (2, 2), which, however, trace only the cooler gas. Spatial densities are typical of IRDCs.

4.1.4. G33.71–0.01

G33.71–0.01 was mapped in NH_3 (1, 1) and (2, 2) by Pillai et al. (2006a); they derived a kinetic temperature of ∼21 K. The methanol spectrum toward the source is characterised by weak non-Gaussian wings at 3 mm and 1 mm, in the $k = 0, -1$ lines. No highly excited lines are detected in any band. The modelling of the source was performed with two components, one to model the wings and the other for the bulk emission. The derived physical parameters are typical of infrared dark clouds, even if the temperatures are slightly higher that values from the NH_3 study Pillai et al. (2006a). This, however, could reflect the fact that the (1, 1) and (2, 2) ammonia lines are not sensitive to the warm gas.

4.1.5. G79.3+0.3 P1

G79.3+0.3 P1 belongs to the larger infrared dark cloud G79.34+0.33. This region shows several signposts of star formation activity, with the HII region DR 15 lying behind it and with spots of warm dust emission between the different sub-cores. P1 is the most prominent condensation of the region; Gemini mid-infrared observations by Redman et al. (2003) reveal three YSOs within the cloud and BIMA 3 mm data suggest that the brightest of these is a Herbig Ae/Be star. Interaction with the IRDC is expected and probably responsible for blue wings seen in the

HCO^+. BIMA observations at 96 GHz (Wyrowski, Priv. Comm.) show that CH_3OH does not peak at the continuum position found in the SCUBA data (Carey et al. 2000), but is offset by ∼–35″ in declination. Since this information was not available at the time our observations were performed, our data were taken toward the SCUBA peak position. The source does show a simple CH_3OH spectrum, with detections only in the lower excitation lines. Line profiles are Gaussian, with narrow linewidths ($\Delta v \sim 2$ km s^{-1}), which may indicate that the source is not very massive. A single component model was used for the source. Physical parameters are typical of infrared dark clouds.

4.2. High-mass protostellar objects

The sources in the HMOPs subsample belong to a larger dataset of HMPOs studied in detail over the recent years by Sridharan et al. (2002) and Beuther et al. (2002a,b,c), in radio and millimetre-wavelength continuum emission, and in several molecular tracers. The sources, which were selected, amongst other criteria, to be bright at mid- and far-infrared wavelengths and not associated with any evolved region, have:

- bolometric luminosities between $10^{3.5}$ and $10^{5.6}$ $L_\odot$;
- average kinetic temperature of 20 K (from the NH_3 (1, 1) and (2, 2) lines);
- average density of 10^6 cm^{-3}.

Recent continuum observations of the sample at 850 μm and 450 μm (Williams et al. 2004) reveal that the dust emissivity spectral index toward these sources is significantly lower than toward UCHII regions (mean values of 0.9 versus 2.0, Williams et al. 2004; Hunter 1997).

4.2.1. IRAS 18089–1732

With a bolometric luminosity of $10^{4.5}$ $L_\odot$ and a massive core, $M > 1000$ $M_\odot$ (Sridharan et al. 2002; Beuther et al. 2002a, 2005a), IRAS 18089–1732 shows several signposts of intense high-mass star formation activity, e.g., H_2O and CH_3OH maser emission (Beuther et al. 2002c) and outflows detected in different molecular tracers (Beuther et al. 2004b). A velocity gradient across the core is found in the $HCOOCH_3$ data that Beuther et al. (2004a, 2005b) interpret as originating from a rotating disk.

Our CH_3OH analysis uses three components along the line of sight. From our 30 m data, we found extended emission in the less excited transitions, whose source size is used for the outer component in the model. High resolution data (Wyrowski, Priv. Comm.; Beuther et al. 2004b) reveal an extended component (2–4″ depending on the transition), which in our model is mainly responsible for the emission in the 25 GHz lines and in $^{13}CH_3OH$. Moreover, the detection of several high excited lines in our data, and by other authors (Beuther et al. 2004b, 2002a), and the relatively narrow linewidths compared, for example, with Orion-KL (Schilke et al. 1997) suggest hot core formation in the interior of the source. BIMA observations of the CH_3CN 6 → 5 band (Wyrowski, priv. comm.) show an unresolved, compact emission, suggesting a hot, optically thick component whose source size and temperature are constrained by the luminosity of the object to around 0.5″. Parameters for the external radiation field, used only for the compact component with a source size of 0.5″, are taken from a fit of the continuum data at 1.2 mm (MAMBO) and 2.7 mm (BIMA) and are equal to a dust opacity index of 1.8 and $\tau_{100\ \mu m} = 1$ (Wyrowski, priv. comm.).

In Sect. 3, we discussed how the higher excitation lines and the $^{13}CH_3OH$ lines can be used as a more reliable probe in hot, complex sources. IRAS 18089 is an example of such a complex source, where several $v_t = 0$ lines of the main isotopologue are optically thick. Constraints on the kinetic temperature comes from the $v_t = 1$ lines. At high column densities, the $J_2 \rightarrow J_1$-E lines mase in a broad range of densities, but their intensities decrease at high density ($n > 10^7$ cm^{-3}) and high temperature ($T_{\rm kin} > 180$ K). The non detection of maser activity in the $J_2 \rightarrow J_1$-E band constrains these parameters to high values.

The physical parameters of component 3 are typical of hot cores, while the other two components have mean HMPOs values. A jump from the extended to the compact component is seen in the abundances derived for methanol. This reflects the increase in their gas temperatures and could be explained by thermal evaporation of the ice mantles of grains (e.g., Menten et al. 1988; van der Tak et al. 2000a).

4.2.2. IRAS 18151–1208

The dust continuum map at 1.3 mm of IRAS 18151–1208 ($L \sim 10^{4.3}$ $L_\odot$) reveals three massive cores, with masses ranging from ∼30 $M_\odot$ to ∼550 $M_\odot$ (Beuther et al. 2005a). CH_3OH maser emission is associated with core 1, which is the sub-source we selected for our analysis. At least two separate outflows are seen in CO and H_2 (Davis et al. 2004), with a high degree of collimation.

The CH_3OH spectrum toward the source is rather simple with no highly excited lines indicating any hot component. However, the $k = \pm2, \pm3$ lines in the $5_k \rightarrow 4_k$ band, with a lower level energy in the ∼60–70 K range, are detected. The $5_{-1} \rightarrow 4_{-1}$-$E$ line at 1.3 mm shows a non-Gaussian profile with a blue-shifted wing. However, no deviations from a Gaussian line profile are seen in the $5_0 \rightarrow 4_0$-A, which has similar excitation conditions as the $k = -1$-E line. Overlap with the HNCO (11-10) series ($E_{\rm low} \sim 58$ K) could lead to the same profile in the $k = -1$-E line. Therefore, no component is used in the model for the outflow. The best-fit model, overlaid on the data, is shown in Figs. 18a–c. Our model gives typical HMPO physical parameters, which are well below typical class II CH_3OH maser conditions. As for G11.11, beam dilution can be responsible for the non-detection of a hotter small component.

4.2.3. IRAS 18182–1433

The bolometric luminosity and mass of IRAS 18182–1433 ($L \sim 10^{4.3}$ $L_\odot$, $M \sim 1500$ $M_\odot$), together with the detection of complex molecules like CH_3CN, CH_3OCH_3 (Leurini & Schilke 2007), suggest that this source is undergoing hot core formation or already hosts a not very massive hot core. Williams et al. (2004, 2005) modelled the continuum emission combining information at different frequencies from MAMBO, SCUBA, and IRAS observations, and found that a dust opacity index of 1.6 and $\tau_{100\ \mu m} = 5$ fit the data well. Recently, Beuther et al. (2006) found one single-peaked source in 1.3 mm continuum data (at a resolution of ∼4″), associated with hot (∼150 K) CH_3CN emission, while VLA observations (Zapata et al. 2006) resolve three components. Henkel et al. (1985) found $^{12}C/^{13}C < 50$ in the inner galactic disk. One of their sources (G19.6-0.2, see their Tables 1 and 2) is close to IRAS 18182–1433 and has a similar velocity. Therefore, in our model, we used the value they found, $^{12}C/^{13}C = 41$.

The CH_3OH spectrum shows Gaussian-like profiles with red and blue-shifted wings in the $k = -1$, 0 lines, probably associated with the outflow detected in CO by Beuther et al. (2002b). Highly excited lines are detected in the ground state

($5_4 \rightarrow 4_4$-A, E, $E_{\rm low} \sim 100$ K), and tentatively in the first torsionally excited level. Three components were used to model the source: one for the outflow, one for the main core, and one for the hotter emission. A jump is found in the methanol abundances derived for the three components, from values typical of dark clouds to hot core values.

4.2.4. IRAS 18264–1152

IRAS 18264–1152 ($L \sim 10^4\ L_\odot$) shows several indicators of high-mass star formation. CO observations reveal a massive outflow (Beuther et al. 2002b) centred on the mm dust peak; both CH_3OH and H_2O maser spots are observed (Beuther et al. 2002c). Detection of CH_3CN (Sridharan et al. 2002) may indicate hot core formation going on in the source. Interferometric cm observations (Zapata et al. 2006) resolve three components.

The emission is strong in almost all millimetre lines; however, no torsionally excited transitions are detected. Blue non-Gaussian wings are detected in the $k = 0, -1$ lines. Maser emission is found 2 km s^{-1} away from the system velocity of the source in the centimetre band in the $J_2 \rightarrow J_1$ lines ($J = 5, 6, 7$), together with broader sub-thermal emission at the system velocity. Since no other methanol emission is found at that velocity, we do not use any component to model the spectrum at this velocity. Three components are used to model the CH_3OH spectra: one for the non-Gaussian emission, a second one for the bulk emission in the less excited lines, and a third one for the highly excited lines.

4.2.5. IRAS 18310–0825

The 1.2 mm continuum emission of IRAS 18310–0825 reveals several cores with different properties (Walsh et al. 1998; Beuther et al. 2002a; Sridharan et al. 2005a). We observed the main millimetre condensation of Beuther et al. (2002a), which has a mass of several solar masses ($M_{\rm far} \sim 8000\ M_\odot$, $M_{\rm near} \sim 2000\ M_\odot$). Our CH_3OH spectra show emission only in lower excitation lines in each band. Non-Gaussian wings are tentatively detected in the 3 mm lines. Therefore, we modelled all the lines with only one component along the line of sight.

4.2.6. IRAS 19410+2336

IRAS 19410+2336 ($\sim 10^4\ L_\odot$) shows H_2O and CH_3OH maser emission at the very centre of the core, where a weak cm continuum source is also detected. Beuther et al. (2002c) interpreted it as optically thin free-free emission and suggested that a recently ignited, not very evolved massive object is at the cluster centre. High spatial resolution observations (Beuther & Schilke 2004) reveal 12 small clusters in the 1.3 mm continuum, each dominated by a massive source and surrounded by a cluster of less massive sources. CO interferometric data resolve at least seven bipolar outflows.

The CH_3OH spectra do not show any torsionally excited transitions. However, all the lines in the $5_k \rightarrow 4_k$ are clearly detected. Therefore, we use a model with two components, one for the bulk emission and a second one responsible for the emission in the higher excitation lines and in the $J_2 \rightarrow J_1 - E$ band. Line profiles are well represented by a Gaussian shape.

Table 6. Mean properties and standard deviations of IRDCs and HMPOs.

	Δv [km s^{-1}]	T_k [K]	$n(H_2)$ [cm^{-3}]	Linear size [pc]
IRDCs				
Extended comp.	3 ± 1	24 ± 7	$3 \times 10^5 \pm 2\ 10^5$	0.2 ± 0.06
Outflow[b]	f10 ± 3	15 ± 5	$6 \times 10^4 \pm 2 \times 10^4$	0.2 ± 0.1
Core	4.3 ± 0.5	47 ± 9	$9 \times 10^5 \pm 6 \times 10^5$	0.05 ± 0.01
IRAS 18310–0825				
Extended comp.	2.4	17	$2\ 10^5$	0.2
HPMPOs				
Extended comp.	3.5 ± 0.7	31 ± 9	$1 \times 10^6 \pm 8 \times 10^5$	0.1 ± 0.03
Outflow[b]	8.7 ± 0.5	19 ± 3	$2 \times 10^5 \pm 1 \times 10^5$	0.2 ± 0.05
Core	4.4 ± 1.1	100 ± 80	$3 \times 10^7 \pm 10^7$	0.02 ± 0.01

[b] Components with $\Delta v > 7$ km s^{-1}.

4.2.7. IRAS 20126+4104

IRAS 20126+4104 ($L \sim 10^4\ L_\odot$) was studied in great detail over the last years (e.g., Cesaroni et al. 1997, 1999; Sridharan et al. 2005b; Lebrón et al. 2006; De Buizer 2007) at different angular resolutions. Cesaroni et al. (1997, 1999) identified an extended region, ~15″ in size, with single dish observations, while, at higher spatial resolution, they were able to resolve the inner part of a bipolar outflow and detect a hot core at the centre of it, with temperature ~200 K and mass ~10 $M_\odot$. They also detected a probable Keplerian disk, around a central object with mass ~7 $M_\odot$ (Cesaroni et al. 2005). Recently, mid- and near-infrared observations (Sridharan et al. 2005b; De Buizer 2007) showed that the infrared emission is not of a simple compact source. Methanol thermal emission is associated with both the extended source and the hot core.

The CH_3OH spectrum toward this source is strong in all the observed transitions, but there is no evidence for emission in the torsionally excited lines. However, lines from only a few, very highly excited levels are in the band we observed and we did not perform any observations on the *lower* excitation lines in the $v_t = 1$ band, which were detected by Cesaroni et al. (2005) with the PdBI. Given the evolved stage of the source, we interpret the features on the red-wing of the $5_{-1} \rightarrow 4_{-1}$-$E$ line as being due to the HNCO($11_{0,11}$–$10_{0,10}$) transition and not to methanol. Our model takes into account two components: one for the bulk emission and one for the hot core.

4.2.8. IRAS 23139+5939

IRAS 23139+5939 ($L \sim 10^{4.4}\ L_\odot$) was studied in different molecular tracers and in the continuum (Sridharan et al. 2002; Beuther et al. 2002a,b). Wouterloot et al. (1988) mapped the cloud in NH_3 (1, 1) and (2, 2) lines and reported a temperature of 29 K; CO observations reveal a bipolar outflow (Wouterloot et al. 1989; Shepherd & Churchwell 1996). Beuther et al. (2002c) reported several H_2O masers spots associated with the mm dust continuum peak, but no CH_3OH maser emission. Our observations reveal a methanol millimetre spectrum characterised by broad non-Gaussian emission in the $k = 0, -1$ lines; no highly excited transitions are detected. Therefore, we analysed the source with a two-component model, one for the non-Gaussian emission and a second for the bulk emission. Temperatures and spatial densities are typical of HMPOs.

5. Discussion

The physical properties of our sample are summarised in Table 6, where the mean values of the kinetic temperature, density, and linear size are listed together with the standard deviations. From our analysis on the methanol spectra towards the IRDC subsample of sources, we often found indications of compact cores (∼0.05 pc) and extended clumps (∼0.2 pc). Broad non-Gaussian emission may indicate outflows. The physical parameters derived for the extended components are typical of infrared dark clouds, with densities ranging between 6×10^4 and 8×10^5 cm^{-3} and kinetic temperatures in the range 18–33 K. In many cases, methanol abundances are higher than dark cloud values, up to $\sim10^{-8}$. For the outflow components, the abundances are high, up to 10^{-7}, but these could be upper limits since we assumed spherical geometry in the calculations. Higher temperatures (35–60 K) are found in the compact cores, which show typical IRDC densities (2×10^5–2×10^6 cm^{-3}). Methanol abundances cover a wide range of values, from typical dark cloud abundances ($\sim10^{-9}$) to higher values (10^{-7}). That IRDCs harbour sites of active star formation is now established by several authors (e.g., Teyssier et al. 2002; Rathborne et al. 2006). For the sources in our sample, maser action in the 22 GHz water line and in 6.7 GHz CH_3OH transition was reported by Pillai et al. (2006b) in G11.11-0.12.

The CH_3OH spectra also suggest emission from multiple components for several HMPOs, which can be identified with extended bulk emission from the clump; a hot, dense core; and, in some cases, an outflow. The physical parameters of the clumps, as inferred from our CH_3OH analysis, are temperatures in the range 17–36 K, densities between 2×10^5 and 3×10^6 cm^{-3}, and methanol abundances typical of cold sources (7×10^{-10}–2×10^{-8}). On the other hand, the cores show physical conditions similar to "hot core" sources near or surrounding high-mass (proto)stellar objects, with densities in excess of 10^6 cm^{-3}, temperatures between 60 and 300 K, and X_{CH_3OH} higher than 10^{-7}. In several sources of the sample, a jump in the methanol abundance from the extended component to the compact is required to fit the spectra.

Beuther et al. (2002a) classified all the HMPOs in our sample, with the exception of IRAS 18310, as evolved, "hot core" type sources, on the base of detection of CH_3CN and the existence of resolved cm continuum emission. However, these sources show a variety of methanol spectra, which can probably be interpreted in the context of a finer evolutionary scenario. Complex spectra (highly excited ground state and torsionally excited lines) are found in sources that are in late evolutionary stages and already harbour hot cores, as indicated by the gas parameters derived from our analysis. While typical values for hot cores are ∼0.1 pc and a few hundred solar masses (Cesaroni et al. 1994), the hot core type sources found in our study are smaller and less massive (Table 6), and are in terms of masses and linear sizes, closer to the hot corinos found in low-mass star forming regions (Maret et al. 2004; Ceccarelli 2004) than to the classical hot cores. Less complex spectra are found in sources in earlier stages of star formation, with gas parameters similar to the ones derived for the IRDC subsample. These conditions are also found in the extended regions around the hot cores of our sample.

To obtain general statistics for our sample, we analysed the density and the CH_3OH abundance derived for our sources as a function of temperature. Results from previous studies on hot cores are not included in our comparison; they often make use of high excitation CS lines (e.g., Cesaroni et al. 1991; Churchwell et al. 1992; Mangum & Wootten 1993; Olmi & Cesaroni 1999), but do not include the infrared pumping in their analysis. Carroll & Goldsmith (1981) showed that this effect is not negligible for CS for infrared source temperatures ≥125 K. Moreover, Schilke et al. (2001) noted that diatomic molecules like CS are not pure density tracers, but they probe the pressure of the gas, $p = n \cdot T$. On the other hand, once the radiative pumping vs. collisions degeneracy is solved by observing torsionally excited lines, CH_3OH transitions are often pure density tracers. Besides this, CH_3OH does not trace only warm, dense gas, as CS, but also cold dense gas, where the upper levels of linear rotors are not excited.

Figure 6a shows our derived densities versus the kinetic temperatures. Each physical component from our fit is plotted separately. The density is shown to increase with the kinetic temperature of the gas and our results are not in disagreement with density profiles $n(H_2) \sim R^{-\alpha}$, with $\alpha = 2$ (spherically symmetric clumps), 1.5 (e.g., Hatchell et al. 2001; Williams et al. 2005). The curves in Fig. 6a, obtained by using $n = n_{\rm inner}\times(\frac{r}{r_{\rm inner}})^{-\alpha}$ and a temperature profile of $T = T_{\rm inner}\times(\frac{r}{r_{\rm inner}})^{-0.4}$, and solving by simple variable substitution (and dividing by $n_{\rm inner}\times(\frac{1}{T_{\rm inner}})^{\frac{\alpha}{0.4}}$), are not fits to the data. They are used for illustration of the predicted behaviour of the density as a function of temperature.

Williams et al. (2005) modelled the dust continuum emission towards six of our HMPO sources. We used the total masses given by Williams et al. (2005) to derive the average densities from their analysis at the radii derived from our CH_3OH analysis and compared the results. Due to an error in the paper, the masses have to be corrected down by a factor 1000 (Fuller, priv. comm.). Our derived densities are consistent with their values within a factor of a few; differences between the results obtained with the two methods are expected, as the LVG analysis on CH_3OH infers local densities while the modelling of Williams et al. (2005) assumes a spherical geometry. Moreover methanol is sensitive to the dense gas ($n > 10^4$ cm^{-3}), while the continuum emission from the dust also traces a more diffuse component.

In Fig. 6a, the envelopes of IRDCs have systematically lower density and temperature than HMPOs, while their inner components overlap, partially, with the HMPOs in the temperature-density plane. From our analysis, HMPOs, which still do not harbour any hot core, and IRDCs look essentially like the same objects. The best example is given by IRAS 18310, whose methanol spectrum is very similar, in linewidths, to G79.34P1, and, in detection rate, to the other IRDC positions as well. Our results fit in the picture described by several authors (e.g., Menten et al. 2005; Rathborne et al. 2006) that infrared dark clouds are the birth environments of high-mass stars; within these clouds, dense cores, like the one we observed in this survey, are found, which have similar sizes and densities to the HMPOs and are in different evolutionary stages, some prior to the HMPO phase, some already in it.

In Fig. 6b the methanol abundances of our sources are studied as a function of the gas temperature. As for the density, X_{CH_3OH} is found to increase with the temperature. This is more clear in the HMPO subsample than in the IRDC sources. This trend can be explained by evaporation of methanol from the mantles of the grains in the high temperature regions. However, no step function predicted by models (van der Tak et al. 1999) is found, but X_{CH_3OH} increases smoothly with the gas temperature. This is probably due to the relatively spatial low resolution of our data, and to the model we used for the analysis, more than being a real physical effect.

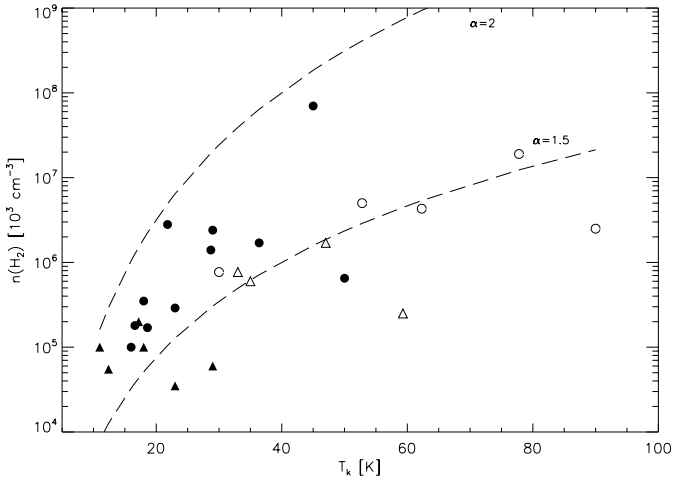

(a)

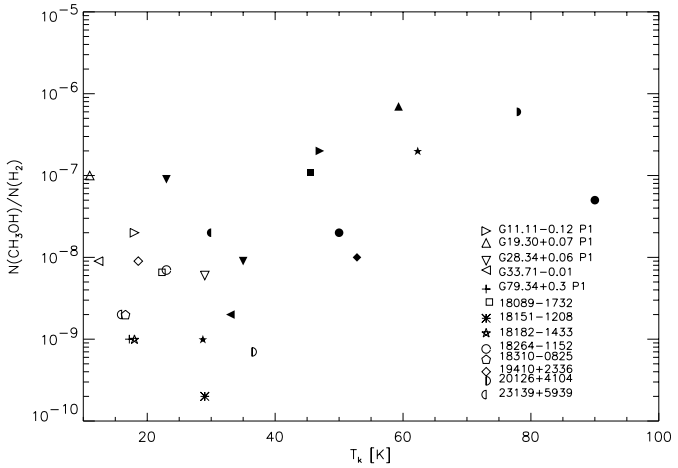

(b)

Fig. 6. The correlation plot of density **a)** and CH_3OH abundance **b)** with the kinetic temperature. In Fig. 6a, the dashed curves represent the density as function of the kinetic temperature assuming a density profile of $n = n_{\rm inner} \times (\frac{r}{r_{\rm inner}})^{-\alpha}$ (with $\alpha = 2$ and 1.5) and a temperature profile of $T = T_{\rm inner} \times (\frac{r}{r_{\rm inner}})^{-0.4}$, which lead to $n = n_{\rm inner} \times (\frac{T}{T_{\rm inner}})^{\frac{\alpha}{0.4}}$. In **a)**, we choose $n_{\rm inner} \times (\frac{1}{T_{\rm inner}})^{\frac{\alpha}{0.4}} = 1$ for convenience. The triangles indicate the IRDCs (full = extended component, open = core) and the circles the HMPOs (full = extended component, open = core). In **b)**, open symbols are used for low abundance components, full ones for the high abundance components.

6. Outlook

We carried out a multi-frequency study of methanol observations of a sample of 13 sources in the early stages of high-mass star formation. Methanol was successfully detected in all the sources of our sample; non-Gaussian profiles were found in several sources in the IDRC and in the HMPO sub-samples, in the $k = 0, \pm 1$ lines. Since SiO observations and other molecular tracers suggest that outflows can be a common phenomenon in these populations of sources, broad, non-Gaussian line shapes detected in CH_3OH can be explained in this context.

Among HMPOs, a variety of different methanol spectra were detected, which probably point out the different evolutionary phases in the sample.

We extended our previous analysis on the excitation mechanisms of methanol to higher energy levels and included the infrared pumping. Our work confirms the usefulness of methanol as a tracer of the physical conditions of the gas phase in high-mass star-forming regions. For the torsional ground state, low excitation lines, which typically have $k \leq 2$ are confirmed to be density tracers, with almost no dependence on the kinetic temperature. Higher excitation lines, at (sub)millimetre wavelengths, are also sensitive to the kinetic temperature. Transitions in the first torsionally excited level are not sensitive to the density, but they are radiatively populated through the FIR field emitted by the dust. We concluded that in hot cores the kinetic temperature and the density can be derived only by observations of the $v_t = 0$ and of the $v_t = 1$ lines. The best candidate for an estimate of the density in hot cores are the CH_3OH transitions at submm frequencies, which have higher critical densities than the mm lines, while the torsionally excited lines are the best tool to derive the temperature.

However, our study also points out the limitations of the analysis we used: methanol is like a *weed*: since it emits over a wide range of physical conditions, it traces very different astronomical environments. To really make use of the full potential of CH_3OH as a probe of dense clouds, it is essential to 1) better characterise the physical environment where methanol emits through high spatial resolution observations; 2) properly model its spectrum including density, temperature distributions, and different geometries for the source structure.

Acknowledgements. We are grateful to the IRAM staff for their support to this project and to A. Kraus for his help on the calibration of the 100 m data. We thank M. Walmsley and F. van der Tak for helpful comments that improved the quality of the paper and E. Polehampton for discussions about the error analysis. Comments by the anonymous referee improved the clarity of this paper. S. L. acknowledges travel support from the Submillimeter Wave Astrophysics Research Group at Caltech.

References

Bachiller, R., Liechti, S., Walmsley, C. M., & Colomer, F. 1995, A&A, 295, L51
Beuther, H., & Schilke, P. 2004, Science, 303, 1167
Beuther, H., Schilke, P., Menten, K. M., et al. 2002a, ApJ, 566, 945
Beuther, H., Schilke, P., Sridharan, T. K., et al. 2002b, A&A, 383, 892
Beuther, H., Walsh, A., Schilke, P., et al. 2002c, A&A, 390, 289
Beuther, H., Hunter, T. R., Zhang, Q., et al. 2004a, ApJ, 616, L23
Beuther, H., Zhang, Q., Hunter, T. R., et al. 2004b, ApJ, 616, L19
Beuther, H., Schilke, P., Menten, K. M., et al. 2005a, ApJ, 633, 535
Beuther, H., Zhang, Q., Sridharan, T. K., & Chen, Y. 2005b, ApJ, 628, 800
Beuther, H., Zhang, Q., Sridharan, T. K., Lee, C.-F., & Zapata, L. A. 2006, A&A, 454, 221
Carey, S. J., Clark, F. O., Egan, M. P., et al. 1998, ApJ, 508, 721
Carey, S. J., Feldman, P. A., Redman, R. O., et al. 2000, ApJ, 543, L157
Carroll, T. J., & Goldsmith, P. F. 1981, ApJ, 245, 891
Cesaroni, R., & Walmsley, C. M. 1991, A&A, 241, 537
Ceccarelli, C. 2004, in ASP Conf. Ser. 195
Cesaroni, R., Churchwell, E., Hofner, P., Walmsley, C. M., & Kurtz, S. 1994, A&A, 288, 903
Cesaroni, R., Felli, M., Testi, L., Walmsley, C. M., & Olmi, L. 1997, A&A, 325, 725
Cesaroni, R., Felli, M., Jenness, T., et al. 1999, A&A, 345, 949
Cesaroni, R., Neri, R., Olmi, L., et al. 2005, A&A, 434, 1039
Cesaroni, R., Walmsley, C. M., Koempe, C., & Churchwell, E. 1991, A&A, 252, 278
Churchwell, E., & Hollis, J. M. 1983, ApJ, 272, 591
Churchwell, E., Walmsley, C. M., & Wood, D. O. S. 1992, A&A, 253, 541
Cragg, D. M., Sobolev, A. M., & Godfrey, P. D. 2005, MNRAS, 360, 533
Davis, C. J., Varricatt, W. P., Todd, S. P., & Ramsay Howat, S. K. 2004, A&A, 425, 981
De Buizer, J. M. 2007, ApJ, 654, L147
De Buizer, J. M., Radomski, J. T., Telesco, C. M., & Piña, R. K. 2005, ApJS, 156, 179
de Jong, T., Dalgarno, A., & Chu, S.-I. 1975, ApJ, 199, 69
Deguchi, S. 1981, ApJ, 249, 145
Egan, M. P., Shipman, R. F., Price, S. D., et al. 1998, ApJ, 494, L199

Faúndez, S., Bronfman, L., Garay, G., et al. 2004, A&A, 426, 97
Friberg, P., Hjalmarson, A., Madden, S. C., & Irvine, W. M. 1988, A&A, 195, 281
Hatchell, J., & van der Tak, F. F. S. 2003, A&A, 409, 589
Hatchell, J., Fuller, G. A., Millar, T. J., Thompson, M. A., & Macdonald, G. H. 2000, A&A, 357, 637
Hatchell, J., Fuller, G. A., & Millar, T. J. 2001, A&A, 372, 281
Hauschildt, H., Gusten, R., Phillips, T. G., et al. 1993, A&A, 273, L23
Henkel, C., Guesten, R., & Gardner, F. F. 1985, A&A, 143, 148
Hill, T., Burton, M. G., Minier, V., et al. 2005, MNRAS, 363, 405
Hunter, T. R. 1997, Ph.D. Thesis
Krügel, E., & Walmsley, C. M. 1984, A&A, 130, 5
Lampton, M., Margon, B., & Bowyer, S. 1976, ApJ, 208, 177
Lebrón, M., Beuther, H., Schilke, P., & Stanke, T. 2006, A&A, 448, 1037
Leurini, S., & Schilke, P. 2007, in preparation
Leurini, S., Schilke, P., Menten, K. M., et al. 2004, A&A, 422, 573
Müller, H. S. P., Thorwirth, S., Roth, D. A., & Winnewisser, G. 2001, A&A, 370, L49
Mangum, J. G., & Wootten, A. 1993, ApJS, 89, 123
Maret, S., Ceccarelli, C., Caux, E., et al. 2004, A&A, 416, 577
Mekhtiev, M. A., Godfrey, P. D., & Hougen, J. T. 1999, J. Mol. Spectrosc., 194, 171
Menten, K., Pillai, T., & Wirowski, F. 2005, in IAU Symp., 23
Menten, K. M., Walmsley, C. M., Henkel, C., & Wilson, T. L. 1986, A&A, 157, 318
Menten, K. M., Walmsley, C. M., Henkel, C., & Wilson, T. L. 1988, A&A, 198, 253
Molinari, S., Brand, J., Cesaroni, R., & Palla, F. 1996, A&A, 308, 573
Molinari, S., Brand, J., Cesaroni, R., Palla, F., & Palumbo, G. G. C. 1998, A&A, 336, 339
Molinari, S., Brand, J., Cesaroni, R., & Palla, F. 2000, A&A, 355, 617
Mueller, K. E., Shirley, Y. L., Evans, N. J., & Jacobson, H. R. 2002, ApJS, 143, 469
Mundy, L. G., Evans, N. J., Snell, R. L., & Goldsmith, P. F. 1987, ApJ, 318, 392
Olmi, L., & Cesaroni, R. 1999, A&A, 352, 266
Perault, M., Omont, A., Simon, G., et al. 1996, A&A, 315, L165
Pillai, T., Wyrowski, F., Carey, S. J., & Menten, K. M. 2006a, A&A, 450, 569
Pillai, T., Wyrowski, F., Menten, K. M., & Krügel, E. 2006b, A&A, 447, 929
Pottage, J. T., Flower, D. R., & Davis, S. L. 2002, J. Phys. B: At. Mol. Phys., 35, 2541
Pottage, J. T., Flower, D. R., & Davis, S. L. 2004, J. Phys. B: At. Mol. Phys., 37, 165
Press, W., Teukolsky, S., Vetterling, W., & Flannery, B. 1992, Numerical Recipes in Fortran The Art of Scientific Computing (Cambridge University Press)
Rathborne, J., Jackson, J., & Simon, R. 2006, ApJ, 641, 389
Redman, R. O., Feldman, P. A., Wyrowski, F., et al. 2003, ApJ, 586, 1127
Schilke, P., Groesbeck, T. D., Blake, G. A., & Phillips, T. G. 1997, ApJS, 108, 301
Schilke, P., Pineau des Forêts, G., Walmsley, C. M., & Martín-Pintado, J. 2001, A&A, 372, 291
Shepherd, D. S., & Churchwell, E. 1996, ApJ, 472, 225
Snell, R. L., Goldsmith, P. F., Erickson, N. R., Mundy, L. G., & Evans, N. J. 1984, ApJ, 276, 625
Sobolev, A. M., & Deguchi, S. 1994, A&A, 291, 569
Sobolev, A. M., Cragg, D. M., & Godfrey, P. D. 1997, A&A, 324, 211
Sridharan, T. K., Beuther, H., Schilke, P., Menten, K. M., & Wyrowski, F. 2002, ApJ, 566, 931
Sridharan, T. K., Beuther, H., Saito, M., Wyrowski, F., & Schilke, P. 2005a, ApJ, 634, L57
Sridharan, T. K., Williams, S. J., & Fuller, G. A. 2005b, ApJ, 631, L73
Tafalla, M., Myers, P. C., Caselli, P., Walmsley, C. M., & Comito, C. 2002, ApJ, 569, 815
Teyssier, D., Hennebelle, P., & Pérault, M. 2002, A&A, 382, 624
van der Tak, F. F. S., van Dishoeck, E. F., Evans, N. J., Bakker, E. J., & Blake, G. A. 1999, ApJ, 522, 991
van der Tak, F. F. S., van Dishoeck, E. F., & Caselli, P. 2000a, A&A, 361, 327
van der Tak, F. F. S., van Dishoeck, E. F., Evans, N. J., & Blake, G. A. 2000b, ApJ, 537, 283
van Zadelhoff, G.-J., Dullemond, C. P., van der Tak, F. F. S., et al. 2002, A&A, 395, 373
Walmsley, C. M., & Ungerechts, H. 1983, A&A, 122, 164
Walmsley, C. M., Menten, K. M., Batrla, W., & Matthews, H. E. 1988, A&A, 197, 271
Walsh, A. J., Burton, M. G., Hyland, A. R., & Robinson, G. 1998, MNRAS, 301, 640
Wilking, B. A., Blackwell, J. H., Mundy, L. G., & Howe, J. E. 1989, ApJ, 345, 257
Williams, S. J., Fuller, G. A., & Sridharan, T. K. 2004, A&A, 417, 115
Williams, S. J., Fuller, G. A., & Sridharan, T. K. 2005, A&A, 434, 257
Wilson, T. L., & Rood, R. 1994, ARA&A, 32, 191
Wouterloot, J. G. A., Walmsley, C. M., & Henkel, C. 1988, A&A, 203, 367
Wouterloot, J. G. A., Henkel, C., & Walmsley, C. M. 1989, A&A, 215, 131
Wyrowski, F., Schilke, P., Walmsley, C. M., & Menten, K. M. 1999, ApJ, 514, L43
Xu, L.-H., & Hougen, J. T. 1995, J. Mol. Spectrosc., 137, 540
Xu, L.-H., & Lovas, F. L. 1997, J. Phys. Chem. Ref. Data, 26, 17
Zapata, L. A., Rodríguez, L. F., Ho, P. T. P., Beuther, H., & Zhang, Q. 2006, AJ, 131, 939

Online Material

Table 7. Integrated intensities and rms for methanol transitions. Empty space indicates non-observations, – non-detections. For IRAS 18089–1732, additional data have been collected in the $7^0_k - 6^0_k$ and $5^1_k - 4^1_k$ $^{12}CH_3OH$ bands (338 and 241 GHz) and in the $2^0_k - 1^0_k$ and $J^0_0 - J^0_{-1}$ $^{13}CH_3OH$ bands (94.4 and 156 GHz). For these observations, the rms is 0.09 K, 0.06 K, 0.02 K, and 0.01 K at 338, 241, 94.4, and 156 GHz respectively. The integrated intensities are 7.1 K km s^{-1} ($7^0_1 \rightarrow 6^0_1$-*E*), 0.7 K km s^{-1} ($1^0_0 \rightarrow 1^0_{-1}$–$^{13}CH_3OH$-*E*), and 0.2 K km s^{-1} ($2^0_{-1} \rightarrow 1^0_{-1}$–$^{13}CH_3OH$-*E*).

	25 GHz		96 GHz		157 GHz		241.7 GHz		255 GHz $^{13}CH_3OH$	
	rms [K]	$\int T_{MB} dv^a$ [K km s^{-1}]	rms [K]	$\int T_{MB} dv^b$ [K km s^{-1}]	rms [K]	$\int T_{MB} dv^c$ [K km s^{-1}]	rms [K]	$\int T_{MB} dv^d$ [K km s^{-1}]	rms [K]	$\int T_{MB} dv^e$ [K km s^{-1}]
G11.11–0.12 P1			0.04	4.5	0.02	0.7	0.05	3.8	0.05	–
G19.30+0.07 P1	0.02	0.4	0.04	12.2	0.03	2.1	0.06	18.9	0.08	–
G28.34+0.06 P1	0.18	0.4	0.04	2.9	0.02	1.2	0.03	8.6	0.03	–
G33.71–0.01	0.15	–	0.03	8.0	0.02	1.2	0.04	8.1	0.03	–
G79.34+0.3 P1			0.03	1.3	0.02	0.3	0.03	0.9	0.03	–
IRAS 18089–1732	0.10	1.0	0.10	5.2	0.05	4.3	0.11	13.4	0.14	1.5
IRAS 18151–1208	0.13	–	0.03	1.5	0.02	1.2	0.05	4.7	0.04	–
IRAS 18182–1433	0.04	0.4	0.05	9.9	0.03	5.3	0.05	18.3	0.05	0.8
IRAS 18264–1152	0.03	0.4	0.04	10.3	0.02	4.9	0.05	23.6	0.05	–
IRAS 18310–0825			0.05	2.7	0.02	0.5	0.05	1.5	0.04	–
IRAS 19410+2336	0.06	0.3[a]	0.04	4.8	0.02	1.9	0.04	6.5	0.04	–
IRAS 20126+4104	0.03	–	0.03	1.8	0.02	1.5	0.04	4.5	0.04	–
IRAS 23139+5939	0.002	–	0.03	4.5	0.03	2.3	0.05	8.3	0.04	–

[a] Integrated intensity of the $2_2 \rightarrow 2_1$-*E* transition. [b] Integrated intensity of the $2_{-1} \rightarrow 1_{-1}$-*E* transition. [c] Integrated intensity of the $2_0 \rightarrow 2_{-1}$-*E* transition. [d] Integrated intensity of the $5_{-1} \rightarrow 4_{-1}$-*E* transition. [d] Integrated intensity of the $8_3 \rightarrow 8_2$-*A* transition of $^{13}CH_3OH$.

Table 8. Integrated intensities of the torsionally excited methanol lines, in IRAS 18089-1732 and IRAS 18182-1433, the only two sources in the sample where the transitions are detected. Empty space indicates non-observations, – indicates non-detections.

		$5^1_1 \rightarrow 4^1_1$-*A* ~ 241.0 GHz	$5^1_k \rightarrow 4^1_k$ ~ 241.2 GHz[a]	$5^1_{-1} \rightarrow 4^1_{-1}$-*A* ~ 241.4 GHz
IRAS 18089–1732	1.3 (rms 0.1 K)	1.17 (rms 0.05 K)	7.03 (rms 0.05 K)	2.21 (rms 0.11 K)
IRAS 18182–1433	–			0.69 (rms 0.05 K)

[a] Not resolved at the resolution of 1.2 km s^{-1}.

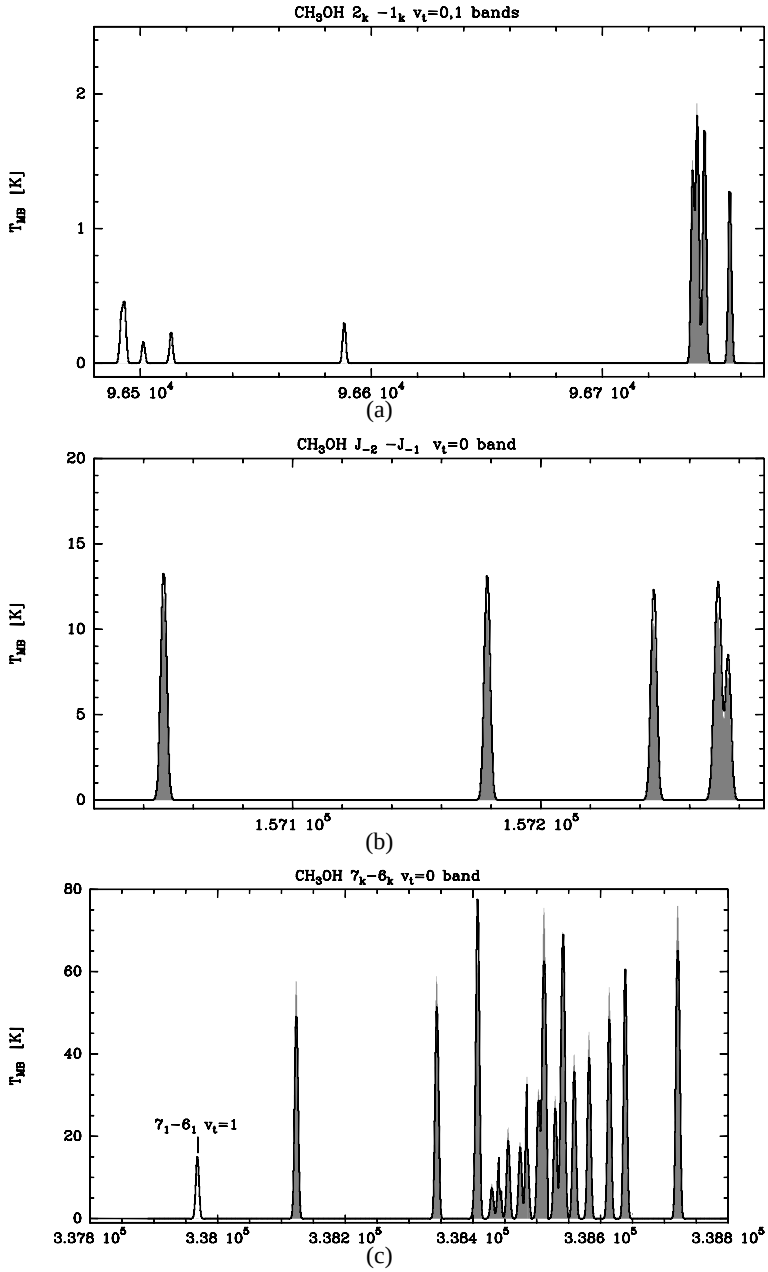

Fig. 7. a)–c) Illustrate how excitation by IR vibrational pumping mimics the effect of collisions in populating the v_t = 0 CH_3OH levels. In grey, synthetic spectra are shown for which pure collisional pumping ($n(H_2)$ = 10^8 cm^{-3}, N_{CH_3OH-E} = N_{CH_3OH-A} = 10^{17} cm^{-2}, no radiation field) is populating the v_t = 0 levels and the v_t = 1 levels; the black line shows the synthetic spectra for the same levels when only the IR radiation field is pumping the system, ($n(H_2)$ = 10^3 cm^{-3}, radiation field given by a grey-body at T_d = 190 K). The synthetic spectra are computed with a source size of 1″, a resolution that can be reached by an interferometer with a baseline of 300 m. While the ground-state spectra are virtually indistinguishable, the v_t = 1 spectra show how inefficiently the pure collisional pumping excites the torsionally excited levels.

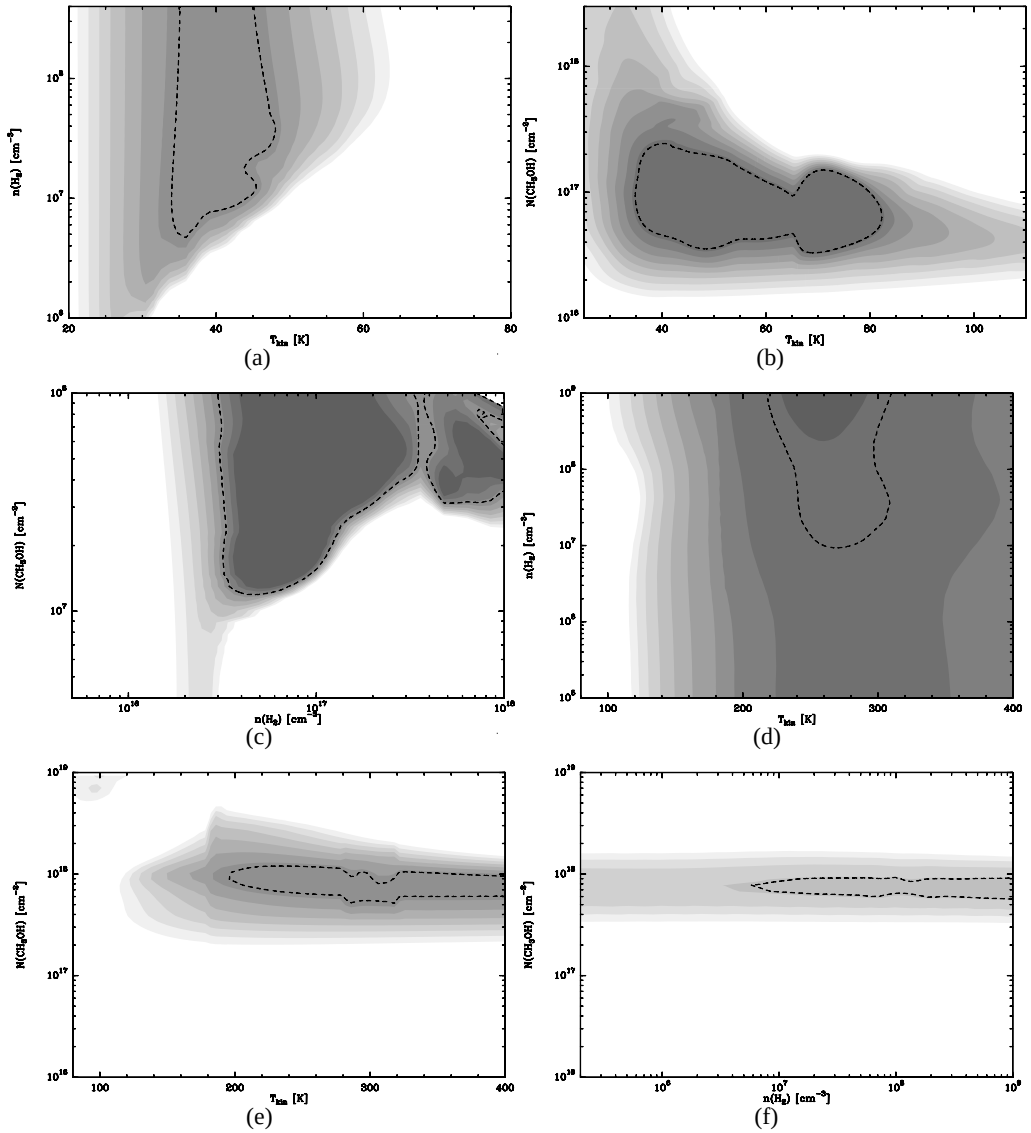

Fig. 8. The χ^2 distribution for IRAS 18089–1732 in the $[T, n]$ **a)**, $[T, N]$ **b)**, $[n, N]$ **c)**, planes for component 2 in Table 4, and for component 3 in the $[T, n]$ **d)**, $[T, N]$ **e)**, $[n, N]$ **f)** planes. All other parameters are fixed to the values of Table 4. The 3σ confidence region lies between the dashed contours.

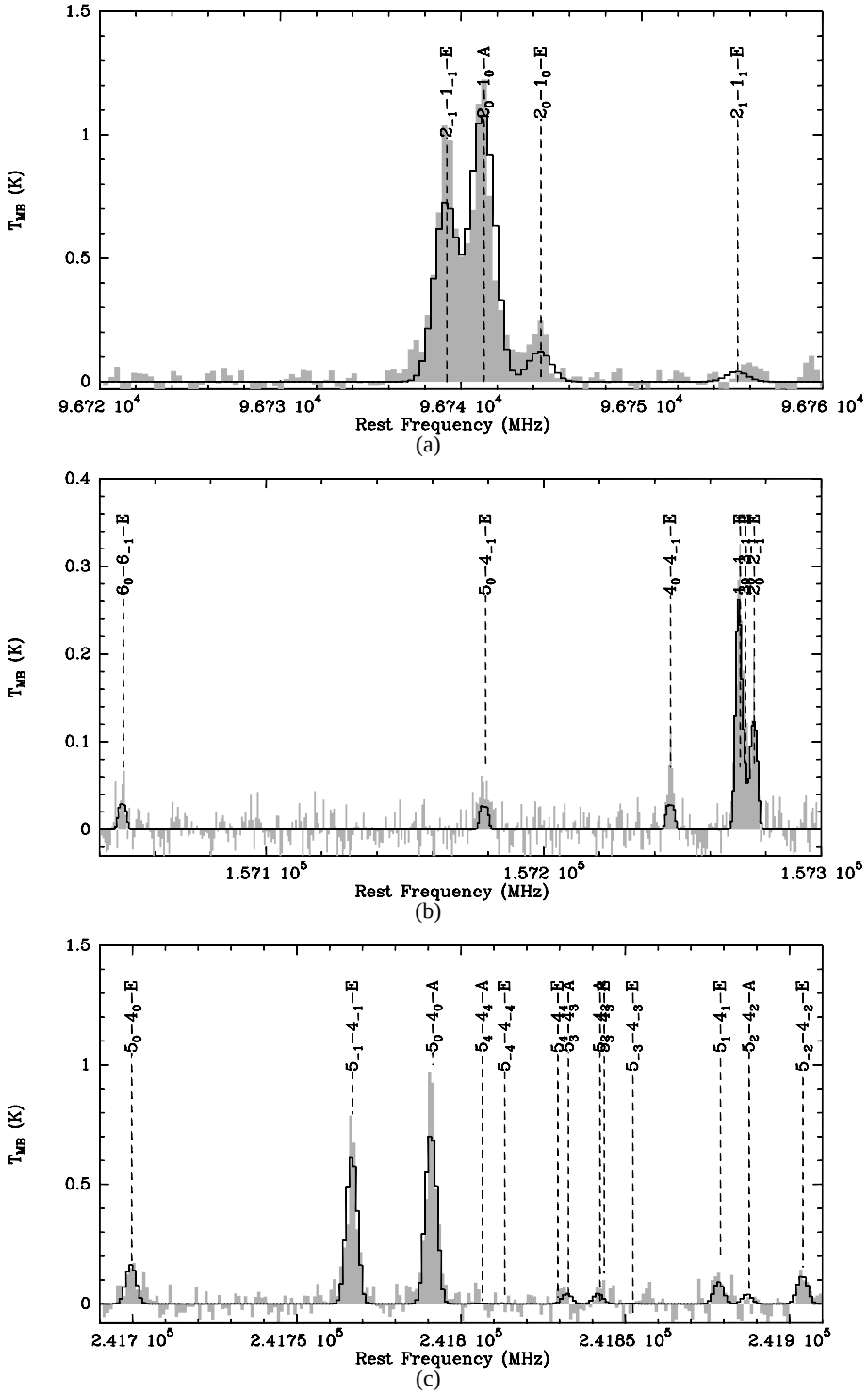

Fig. 9. Spectra toward G11.11P1 taken with the IRAM 30 m telescope. The 1 mm and 2 mm data are smoothed to the resolution of the 3 mm spectra **a)**. All observed lines are labelled. The synthetic spectra resulting from the fit are overlaid in black.

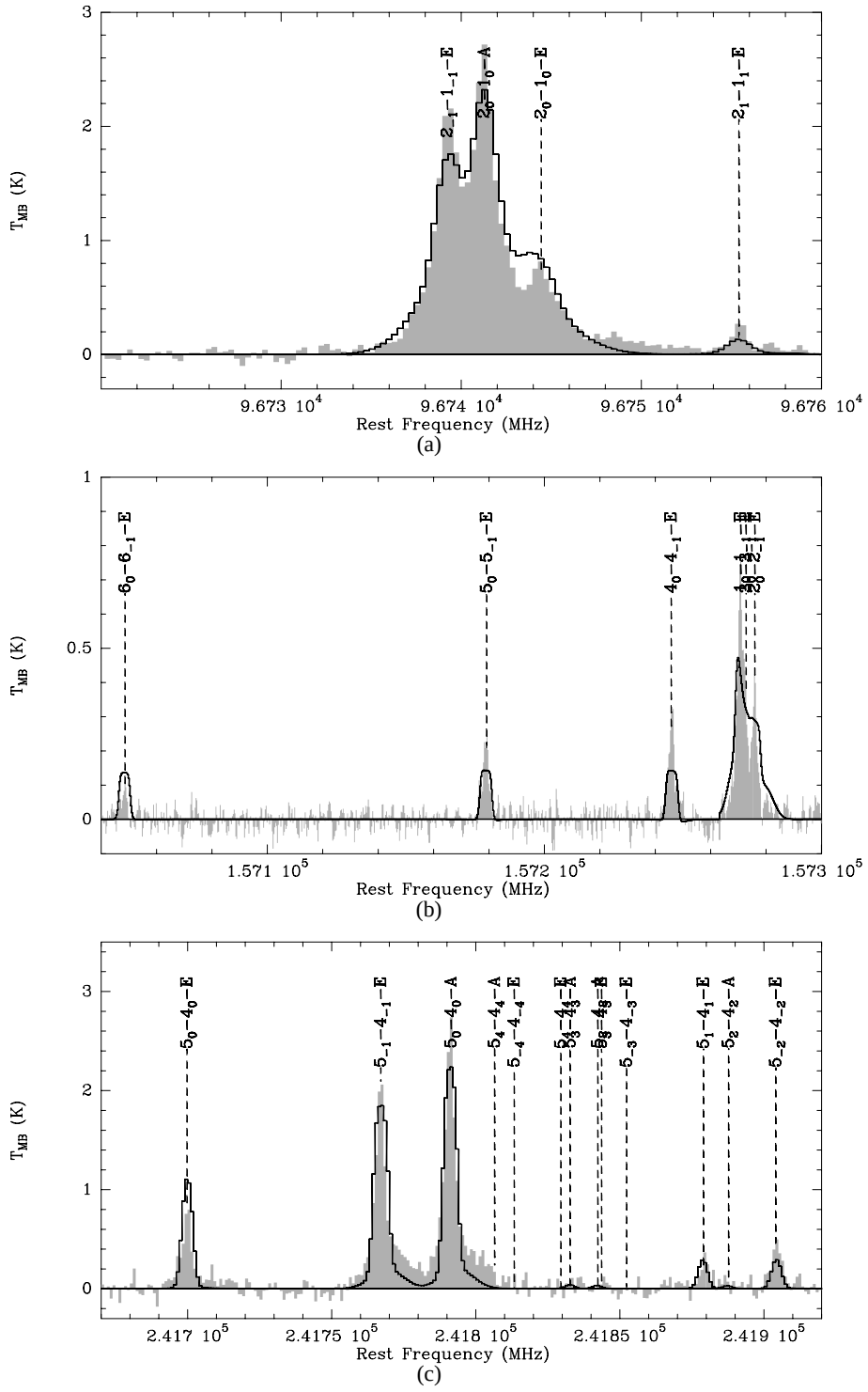

Fig. 10. Spectra toward G19.30P1 taken with the IRAM 30 m telescope. The 1 mm and 2 mm data are smoothed to the resolution of the 3 mm spectra **a)**. All observed lines are labelled. The synthetic spectra resulting from the fit are overlaid in black.

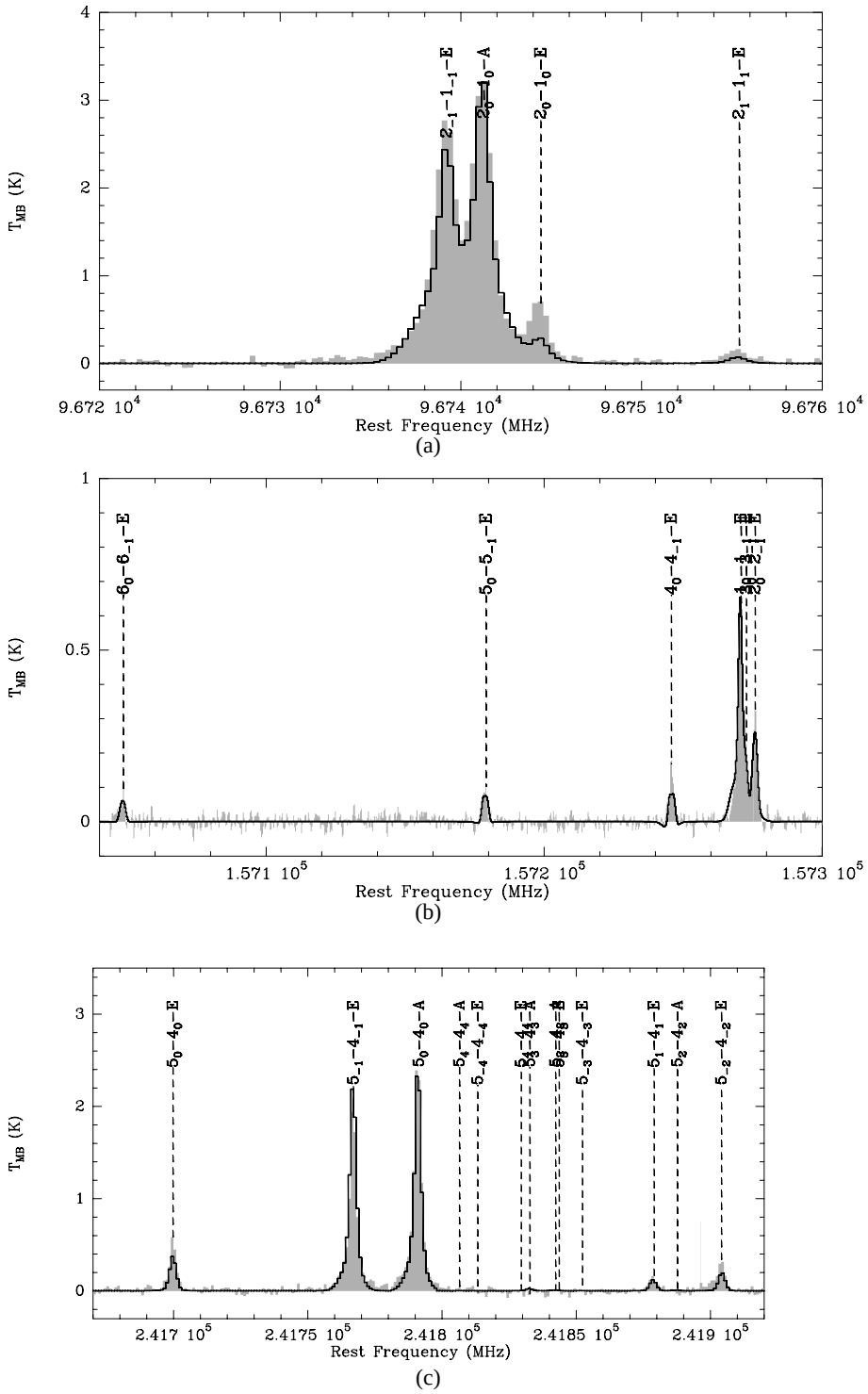

Fig. 11. Spectra toward G28.34 taken with the IRAM 30 m telescope. The 1 mm and 2 mm data are smoothed to the resolution of the 3 mm spectra **a)**. All observed lines are labelled. The synthetic spectra resulting from the fit are overlaid in black.

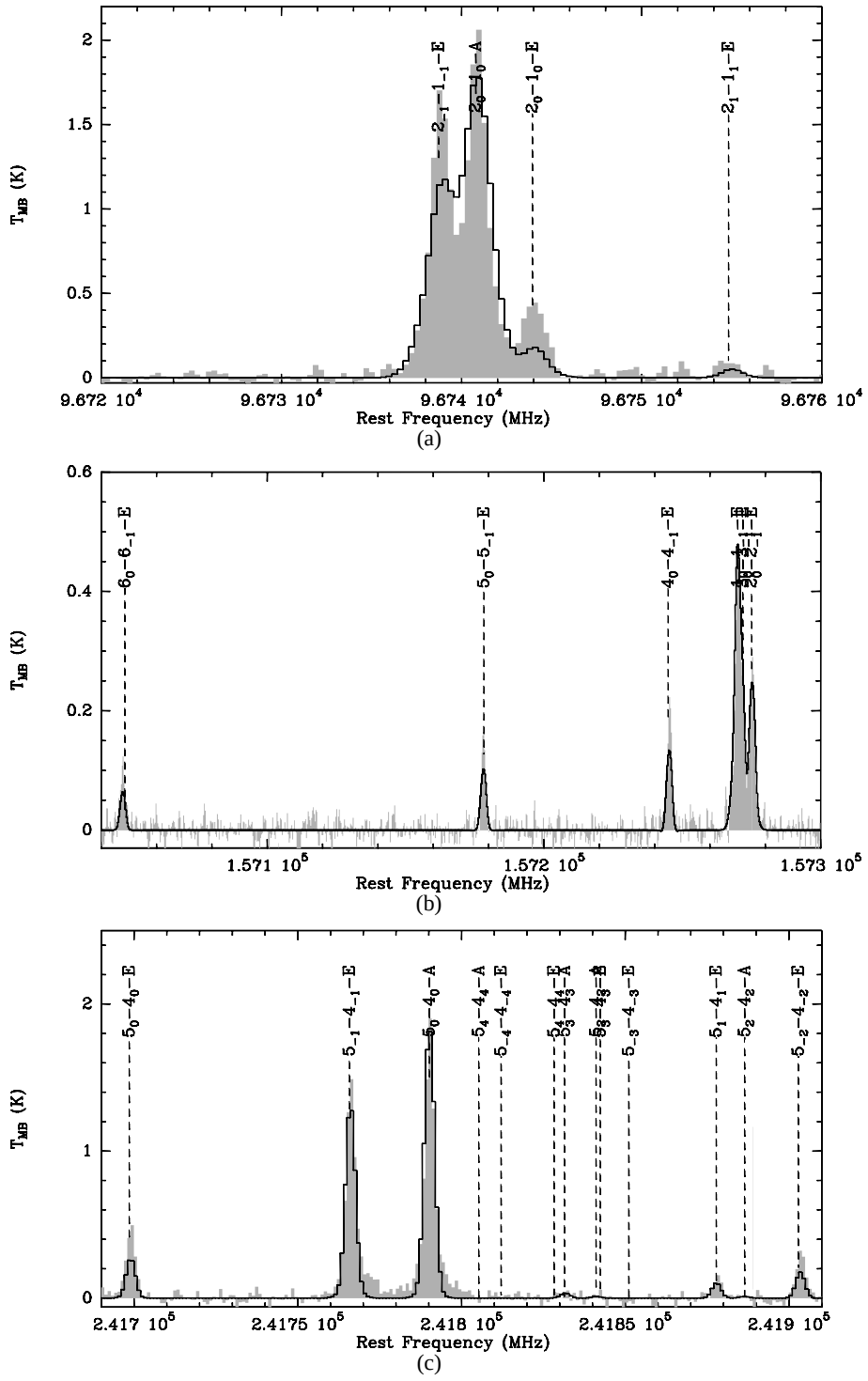

Fig. 12. Spectra toward G33.71 taken with the IRAM 30 m telescope. The 1 mm and 2 mm data are smoothed to the resolution of the 3 mm spectra **a)**. All observed lines are labelled. The synthetic spectra resulting from the fit are overlaid in black.

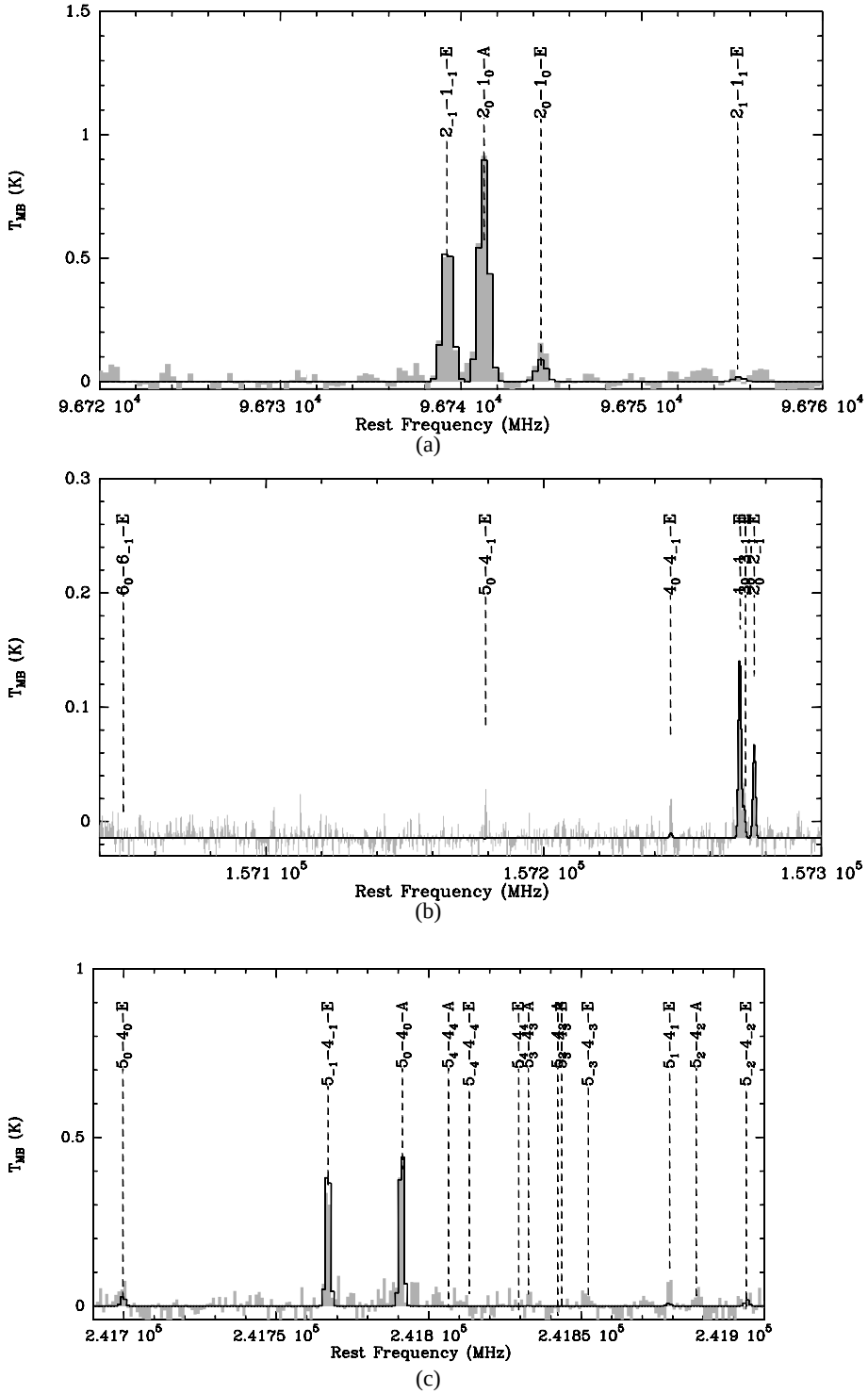

Fig. 13. Spectra toward G79.34P1 taken with the IRAM 30 m telescope. The 1 mm and 2 mm data are smoothed to the resolution of the 3 mm spectra **a)**. All observed lines are labelled. The synthetic spectra resulting from the fit are overlaid in black.

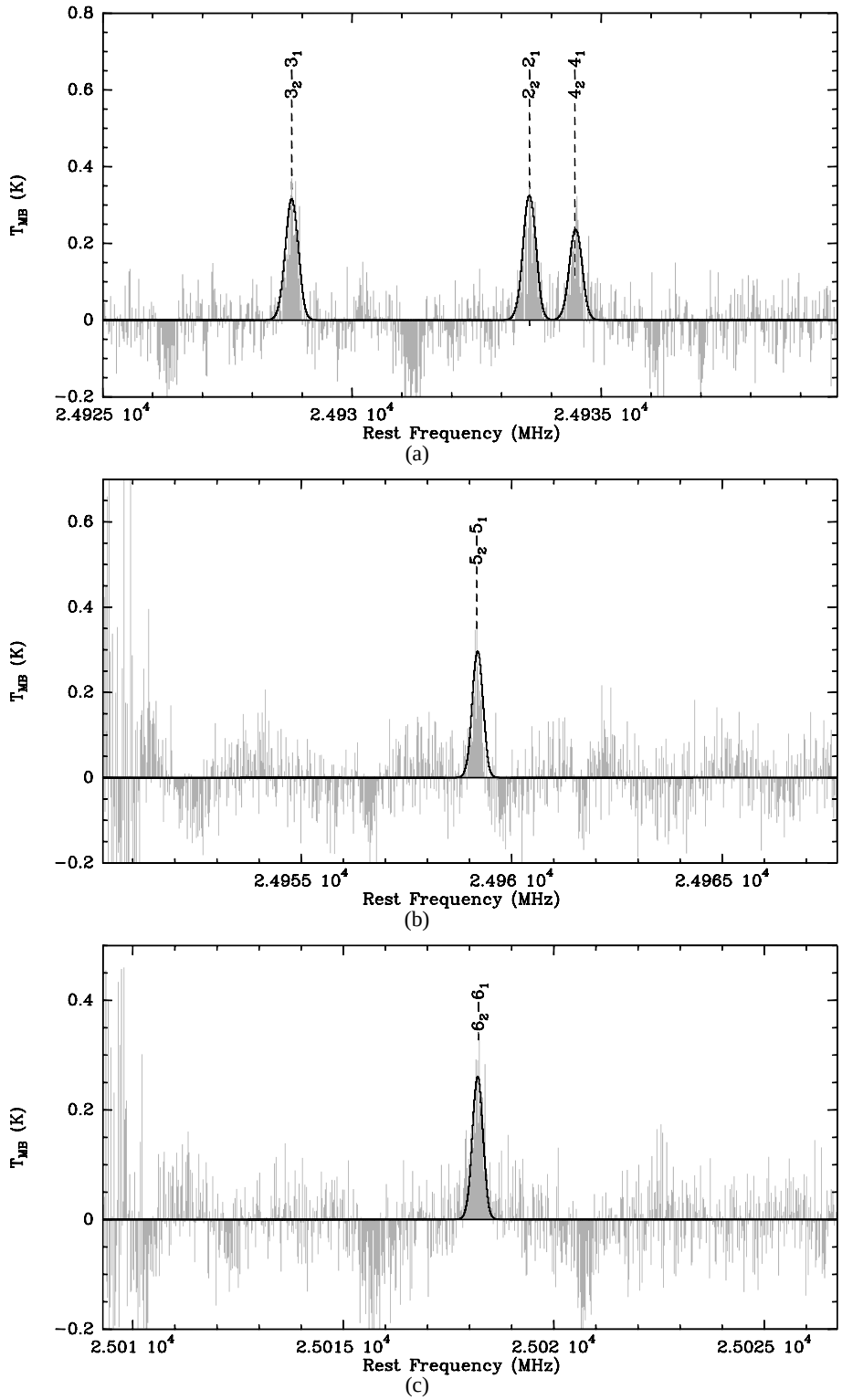

Fig. 14. Spectra toward IRAS 18089–1732 taken with the 100 m telescope, in frequency switching. All observed lines are labelled. The synthetic spectra resulting from the fit are overlaid in black.

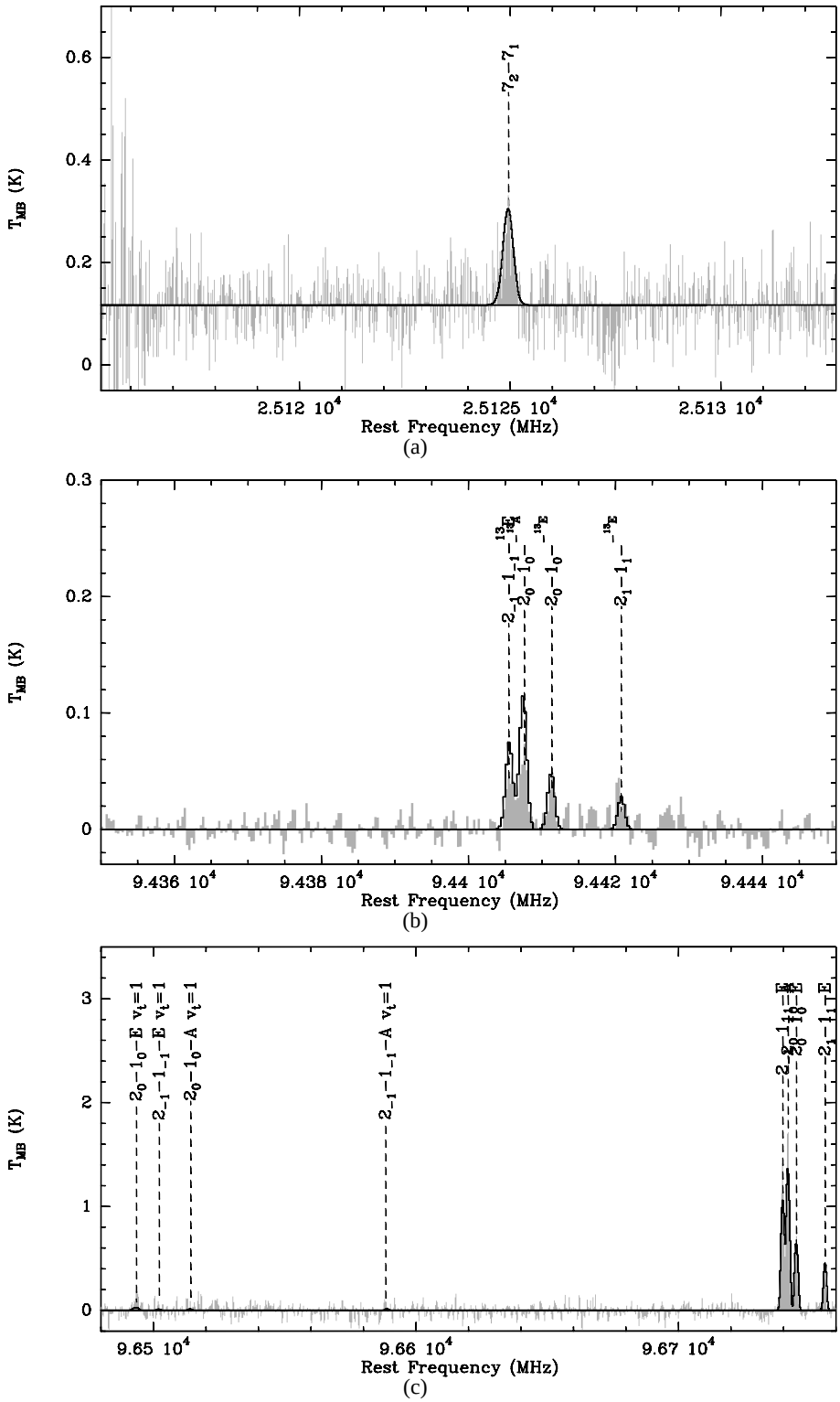

Fig. 15. Spectra toward IRAS 18089–1732 taken with the 100 m telescope (**a)**), in frequency switching, and with the IRAM 30 m telescope (**b)–c)**); the 2 mm data are are smoothed to the resolution of the 3 mm spectra. All observed lines are labelled. The synthetic spectra resulting from the fit are overlaid in black.

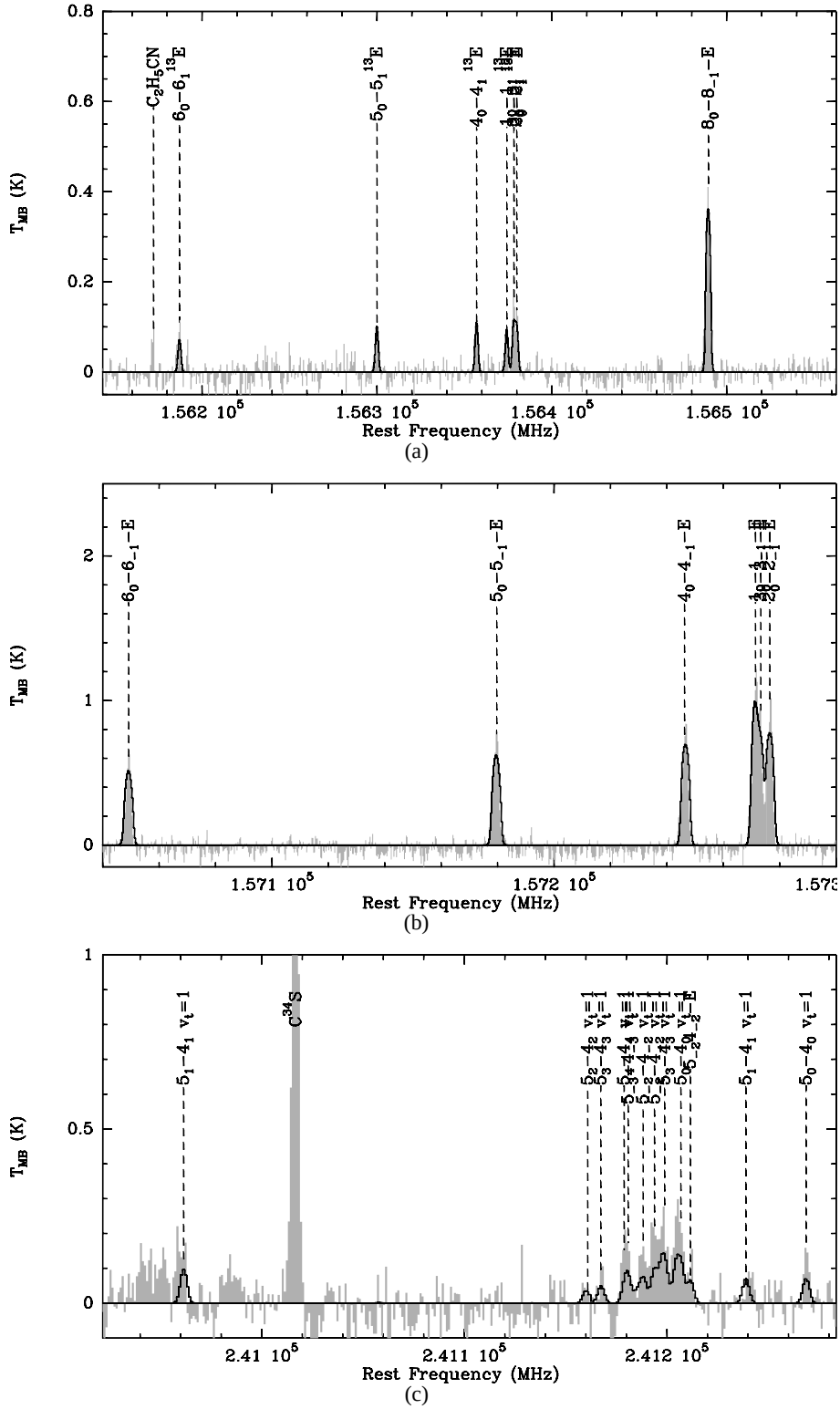

Fig. 16. Spectra toward IRAS 18089–1732 taken with the IRAM 30 m telescope, are smoothed to the resolution of the 3 mm spectra (Fig. 15 **b)**, **c)**. All observed lines are labelled. The synthetic spectra resulting from the fit are overlaid in black.

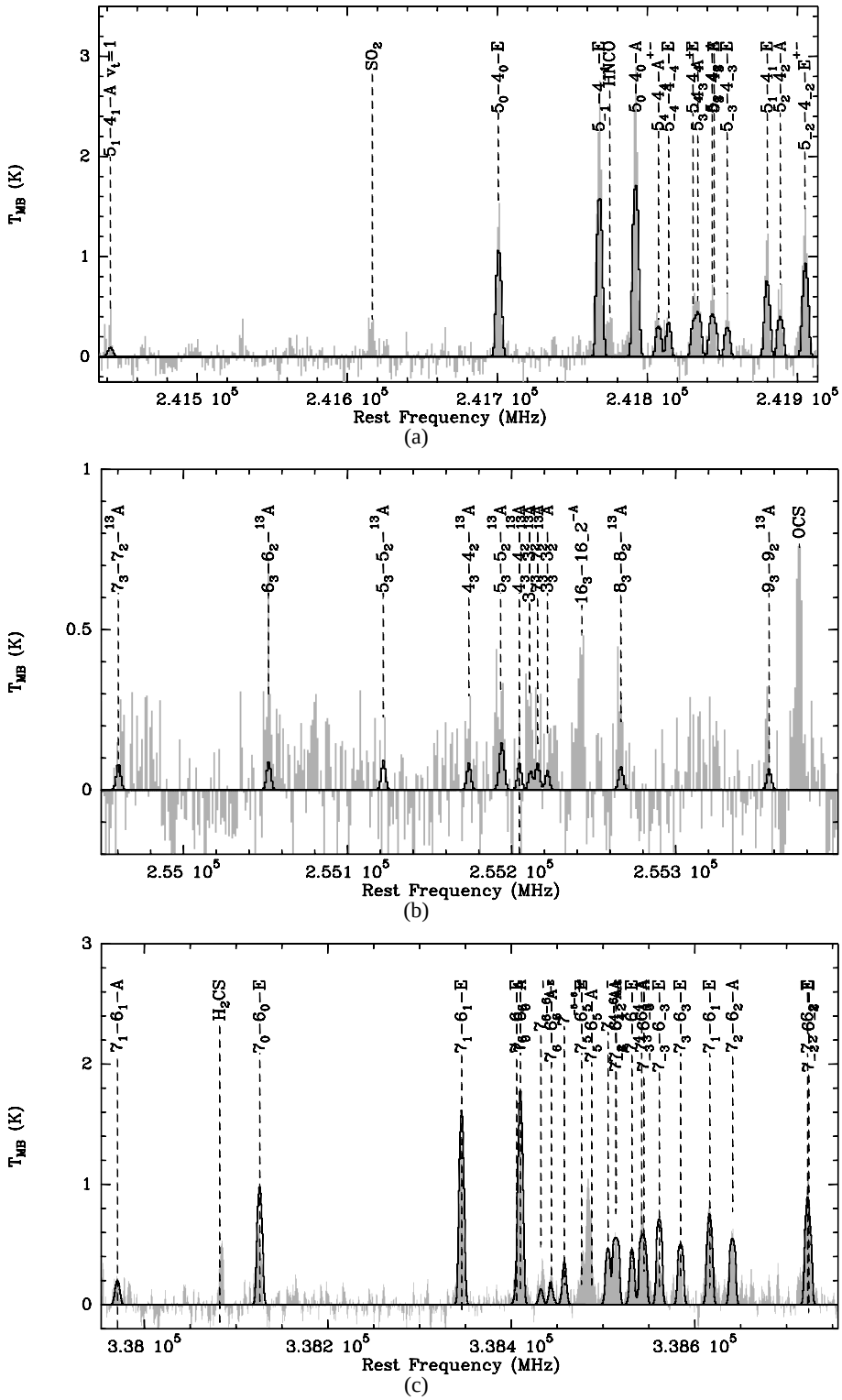

Fig. 17. Spectra toward IRAS 18089–1732 taken with the IRAM 30 m telescope **b)** and with the CSO **c)**, are smoothed to the resolution of the 3 mm spectra **b)**, **c)**. All observed lines are labelled. The synthetic spectra resulting from the fit are overlaid in black. In **c)**, part of the spectrun is not fitted due to contamination from the upper side band.

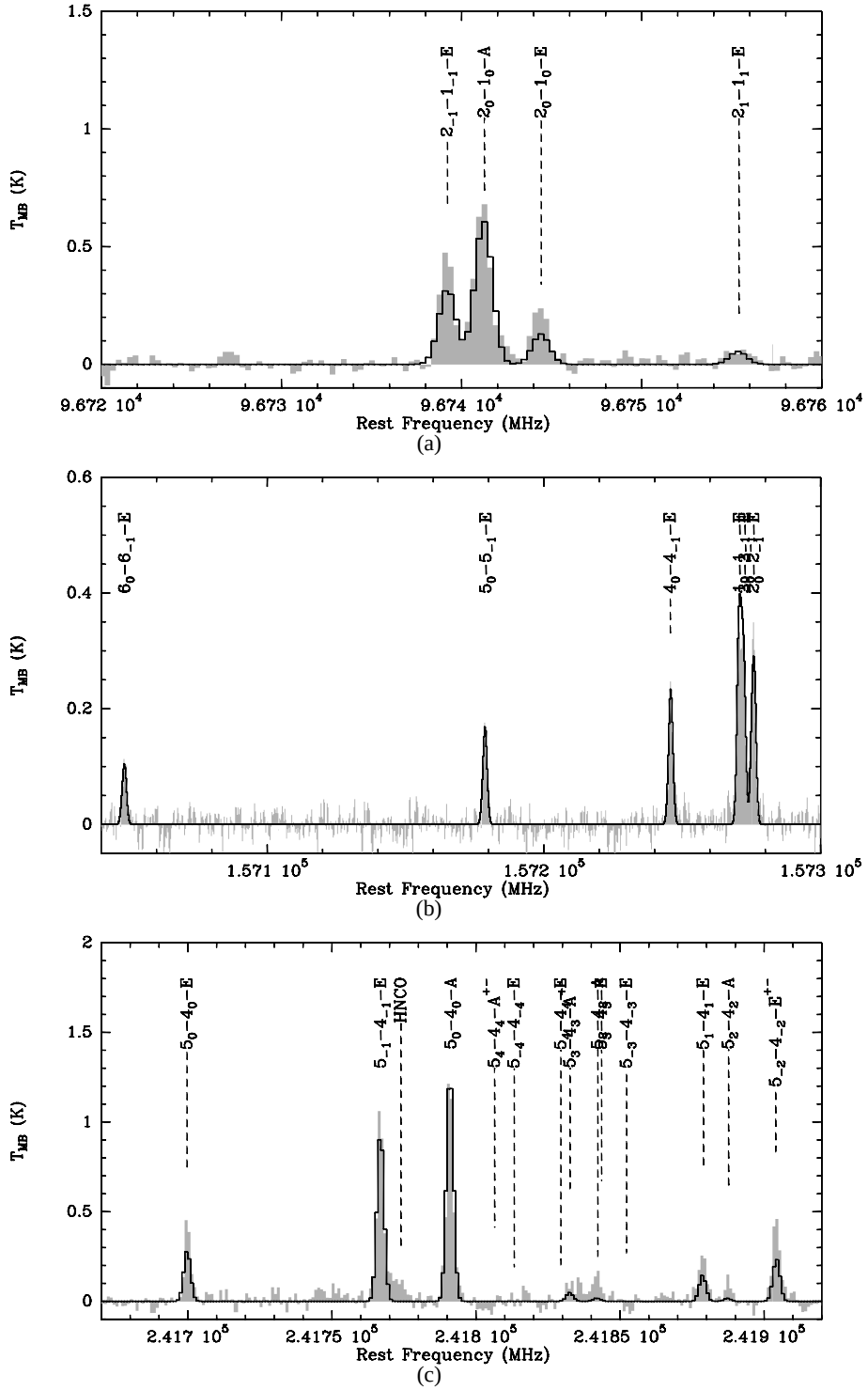

Fig. 18. Spectra toward IRAS 18151–1208 taken with the IRAM 30 m telescope. The 1 mm and 2 mm data are smoothed to the resolution of the 3 mm spectra **a)**. All observed lines are labelled. The synthetic spectra resulting from the fit are overlaid in black.

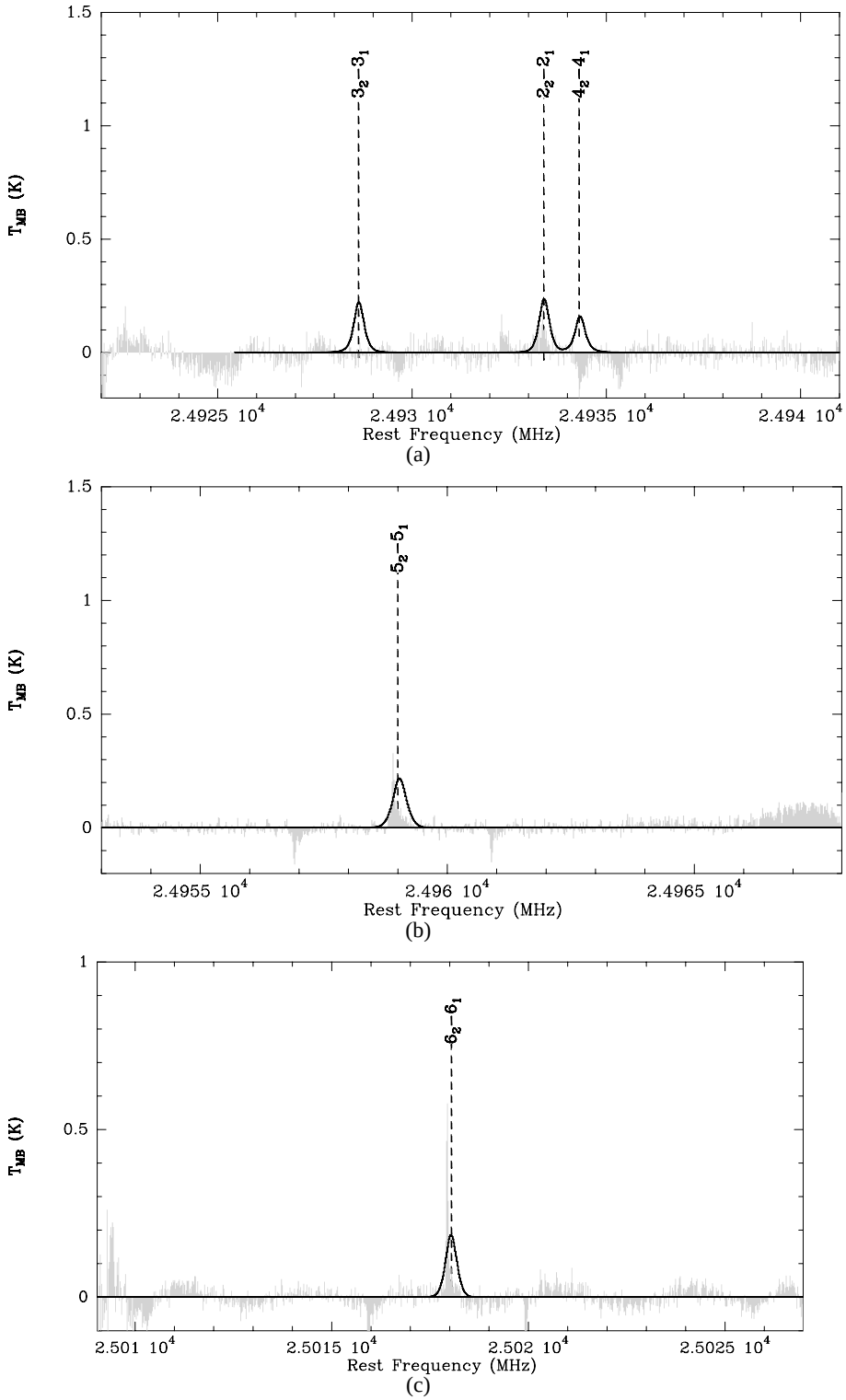

Fig. 19. Spectra toward IRAS 18182−1433 taken with the 100 m telescope, in frequency switching. All observed lines are labelled. The synthetic spectra resulting from the fit are overlaid in black. In **b)** and **c)**, a maser component is probably detected at a different velocity than the system velocity. For the 25 GHz lines, the spectrum overlaid on the data corresponds to the model predictions for this band, which was not included in the analysis.

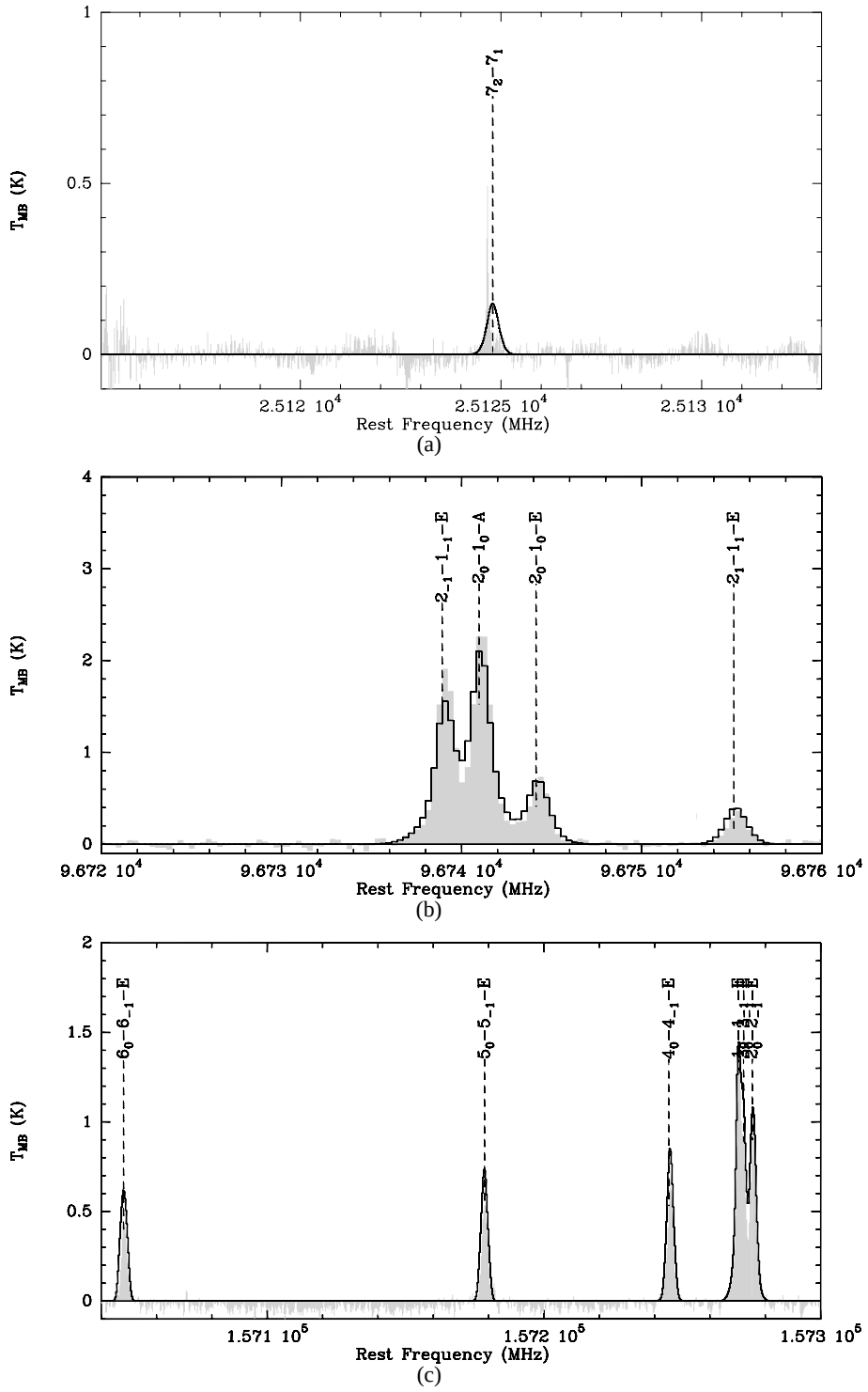

Fig. 20. Spectra toward IRAS 18182–1433 taken with the 100 m telescope **a)**, in frequency switching, and with the IRAM 30 m telescope **b)**, **c)**; the 2 mm data are are smoothed to the resolution of the 3 mm spectra. All observed lines are labelled. The synthetic spectra resulting from the fit are overlaid in black. In **b)**, a maser component is probably detected at a different velocity than the system velocity. For the 25 GHz lines, the spectrum overlaid on the data corresponds to the model predictions for this band, which was not included in the analysis.

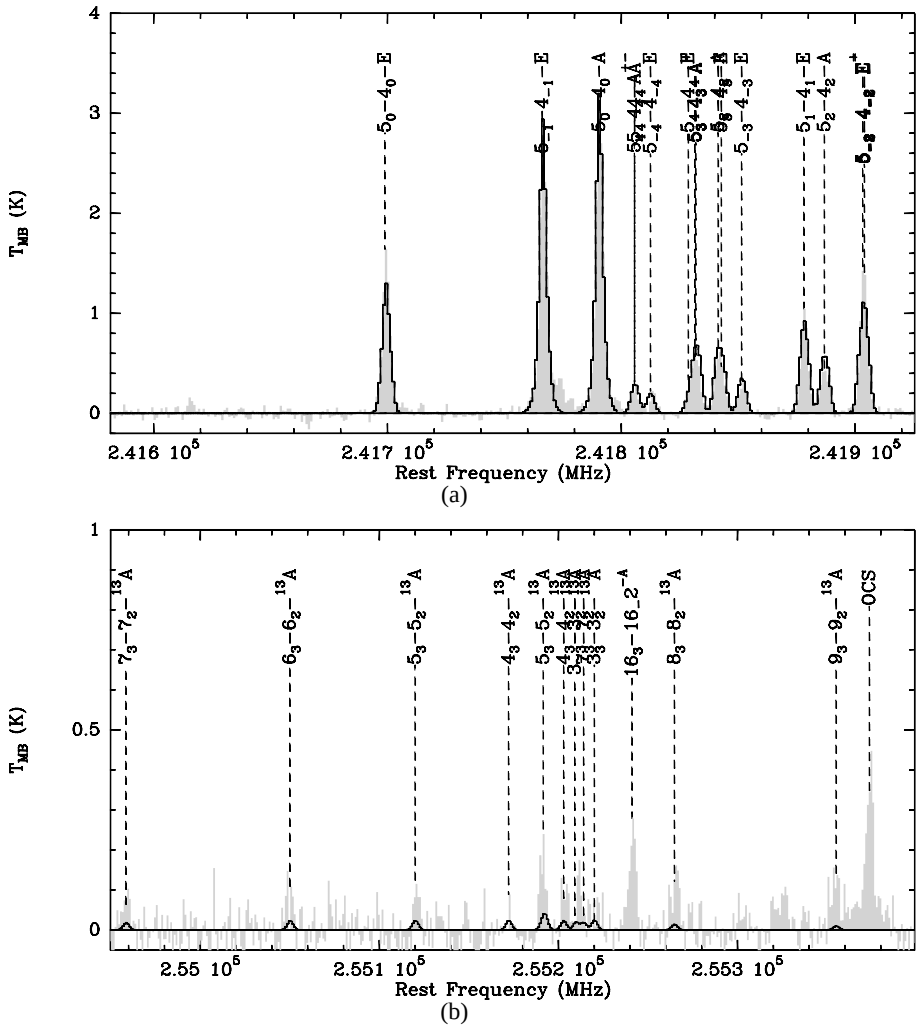

Fig. 21. Spectra toward IRAS 18182–1433 taken with with the IRAM 30 m telescope; data are are smoothed to the resolution of the 3 mm spectra. All observed lines are labelled. The synthetic spectra resulting from the fit are overlaid in black.

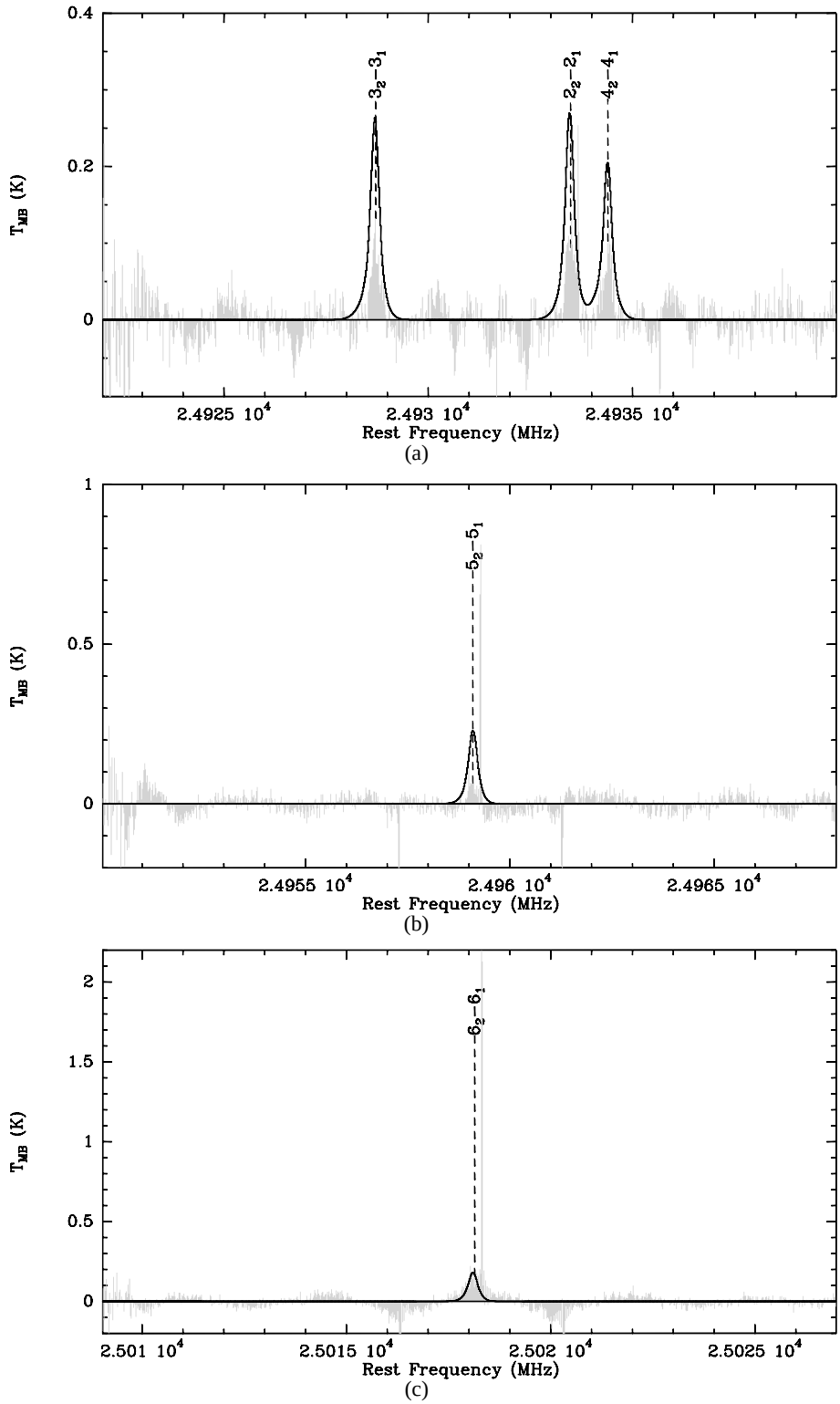

Fig. 22. Spectra toward IRAS 18264–1152 taken with the 100 m telescope, in frequency switching. All observed lines are labelled. The synthetic spectra resulting from the fit are overlaid in black. In Fig. 22**b)** and **c)**, a maser component is detected at a different velocity than the system velocity. For the 25 GHz lines, the spectrum overlaid on the data corresponds to the model predictions for this band, which was not included in the analysis.

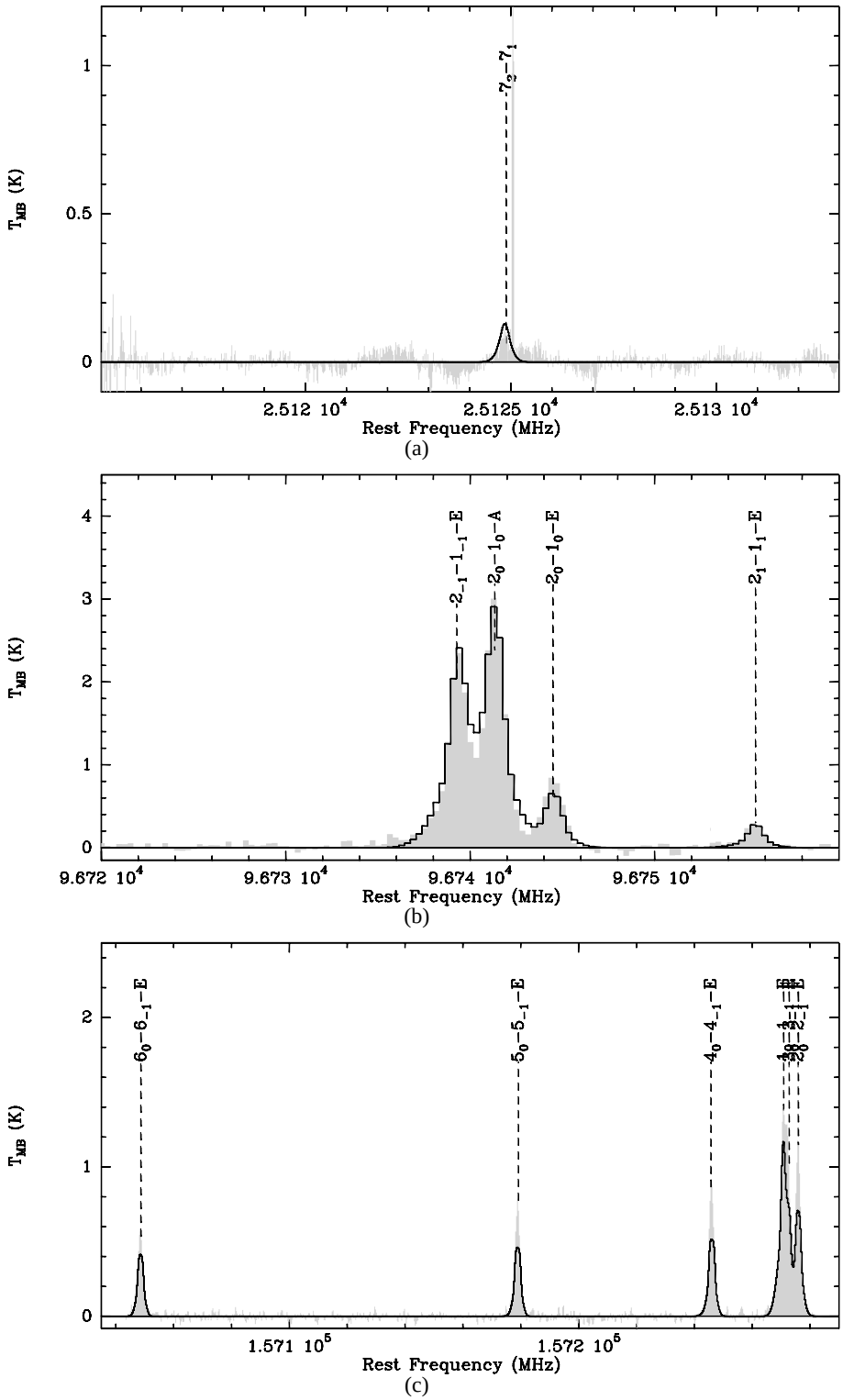

Fig. 23. Spectra toward IRAS 18264–1152 taken with the 100 m telescope **a)**, in frequency switching, and with the IRAM 30 m telescope **b)**, **c)**; the 2 mm data are are smoothed to the resolution of the 3 mm spectra. All observed lines are labelled. The synthetic spectra resulting from the fit are overlaid in black. In **a)**, a maser component is detected at a different velocity than the system velocity. For the 25 GHz lines, the spectrum overlaid on the data corresponds to the model predictions for this band, which was not included in the analysis.

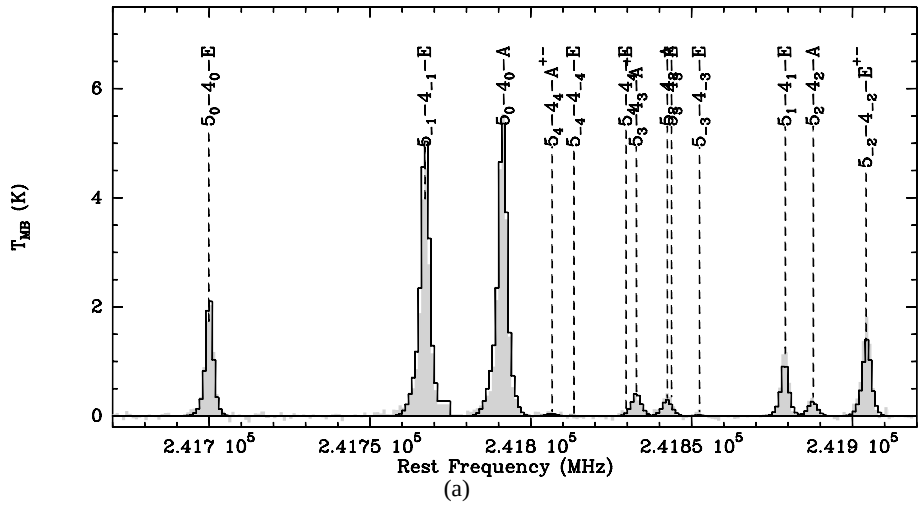

(a)

Fig. 24. 1 mm spectrum toward IRAS 18264–1152 taken with the IRAM 30 m telescope; data are are smoothed to the resolution of the 3 mm spectra (Fig. 23b)). All observed lines are labelled. The synthetic spectra resulting from the fit are overlaid in black.

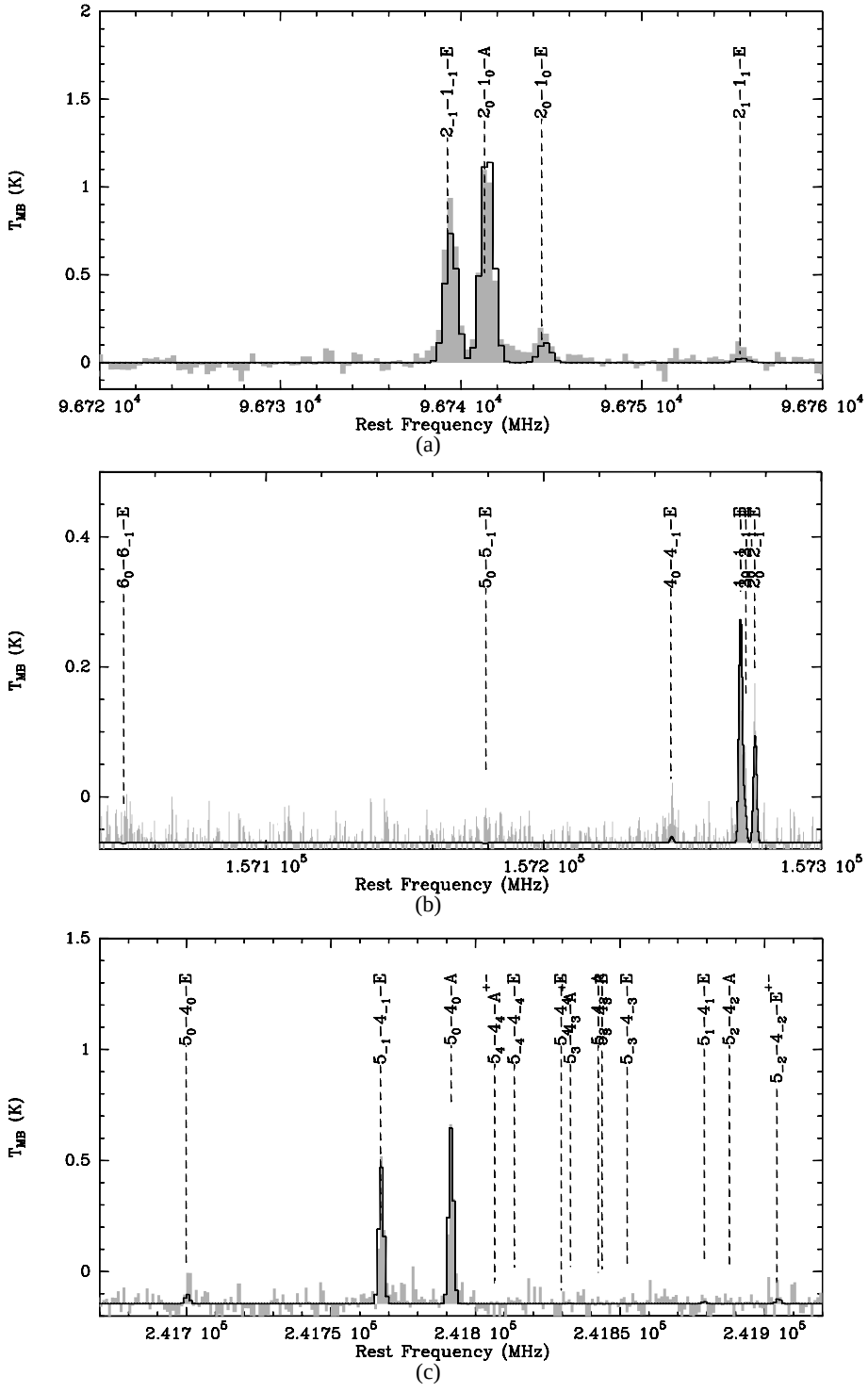

Fig. 25. Spectra toward IRAS 18310–0825 taken with the IRAM 30 m telescope. The 1 mm and 2 mm data are smoothed to the resolution of the 3 mm spectra **a)**. All observed lines are labelled. The synthetic spectra resulting from the fit are overlaid in black.

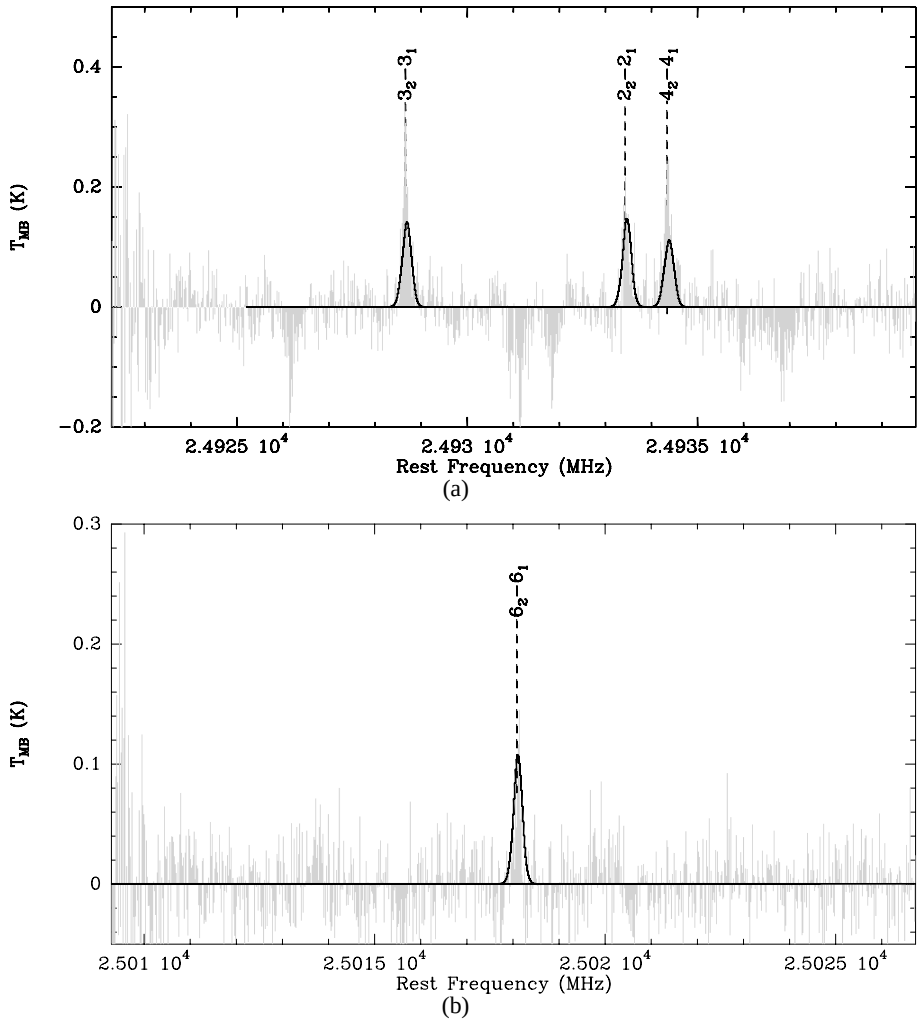

Fig. 26. Spectra toward IRAS 19410+2336 taken with the 100 m telescope, in frequency switching,. All observed lines are labelled. The synthetic spectra resulting from the fit are overlaid in black.

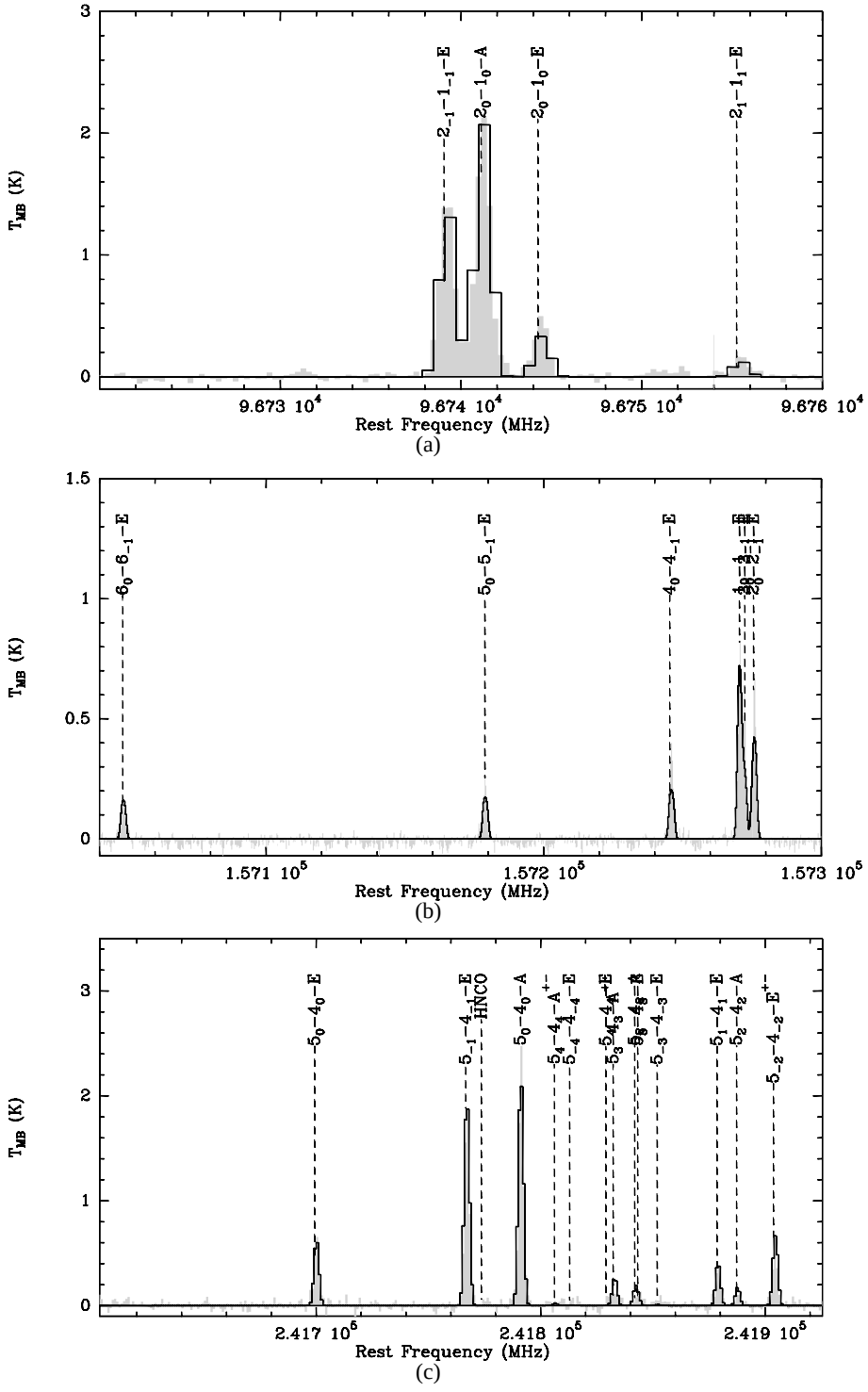

Fig. 27. Spectra toward IRAS 19410+2336 taken with the IRAM 30 m telescope. The 1 mm and 2 mm data are smoothed to the resolution of the 3 mm spectra **a)**. All observed lines are labelled. The synthetic spectra resulting from the fit are overlaid in black.

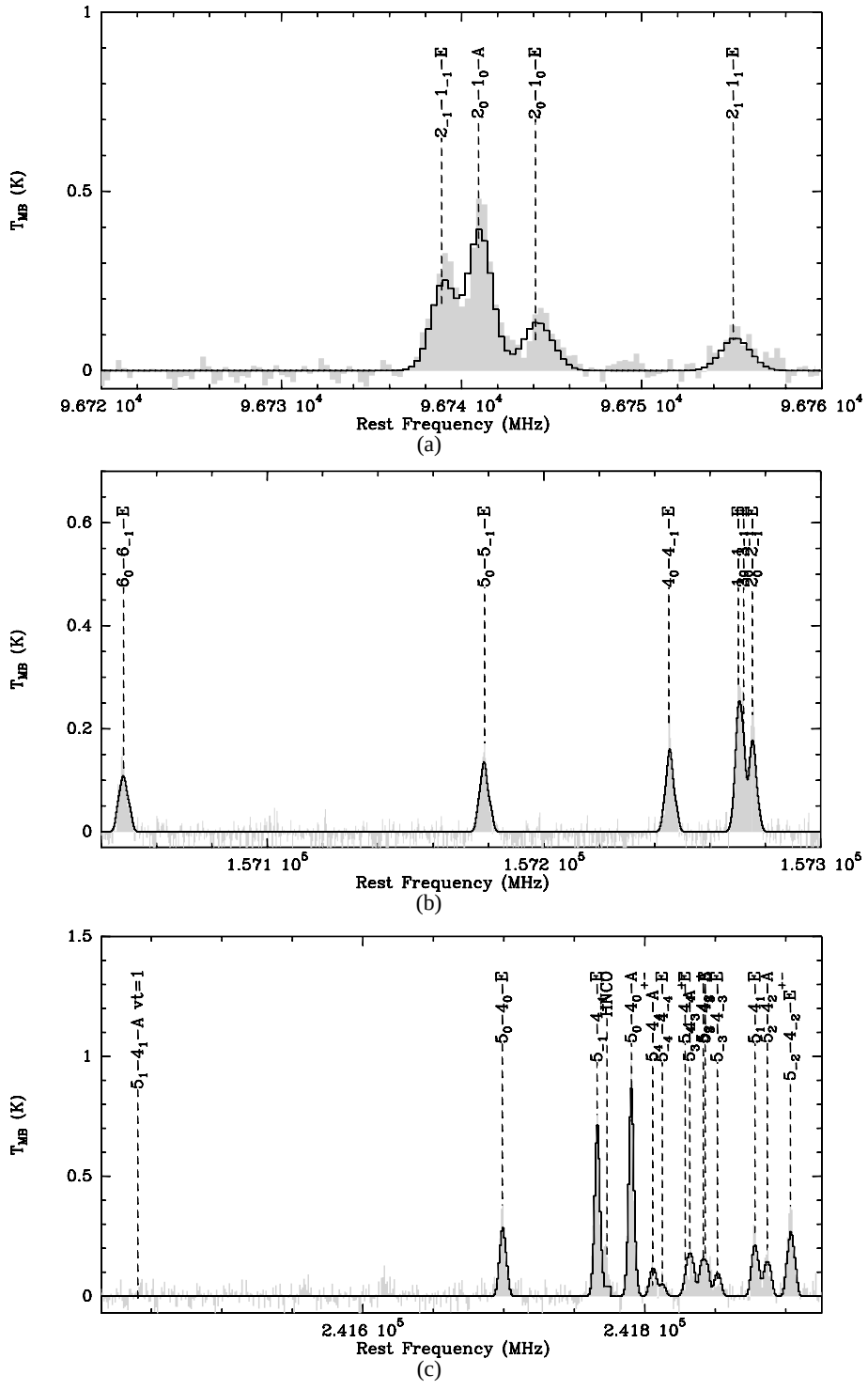

Fig. 28. Spectra toward IRAS 20126+4104 taken with the IRAM 30 m telescope. The 1 mm and 2 mm data are smoothed to the resolution of the 3 mm spectra **a)**. All observed lines are labelled. The synthetic spectra resulting from the fit are overlaid in black.

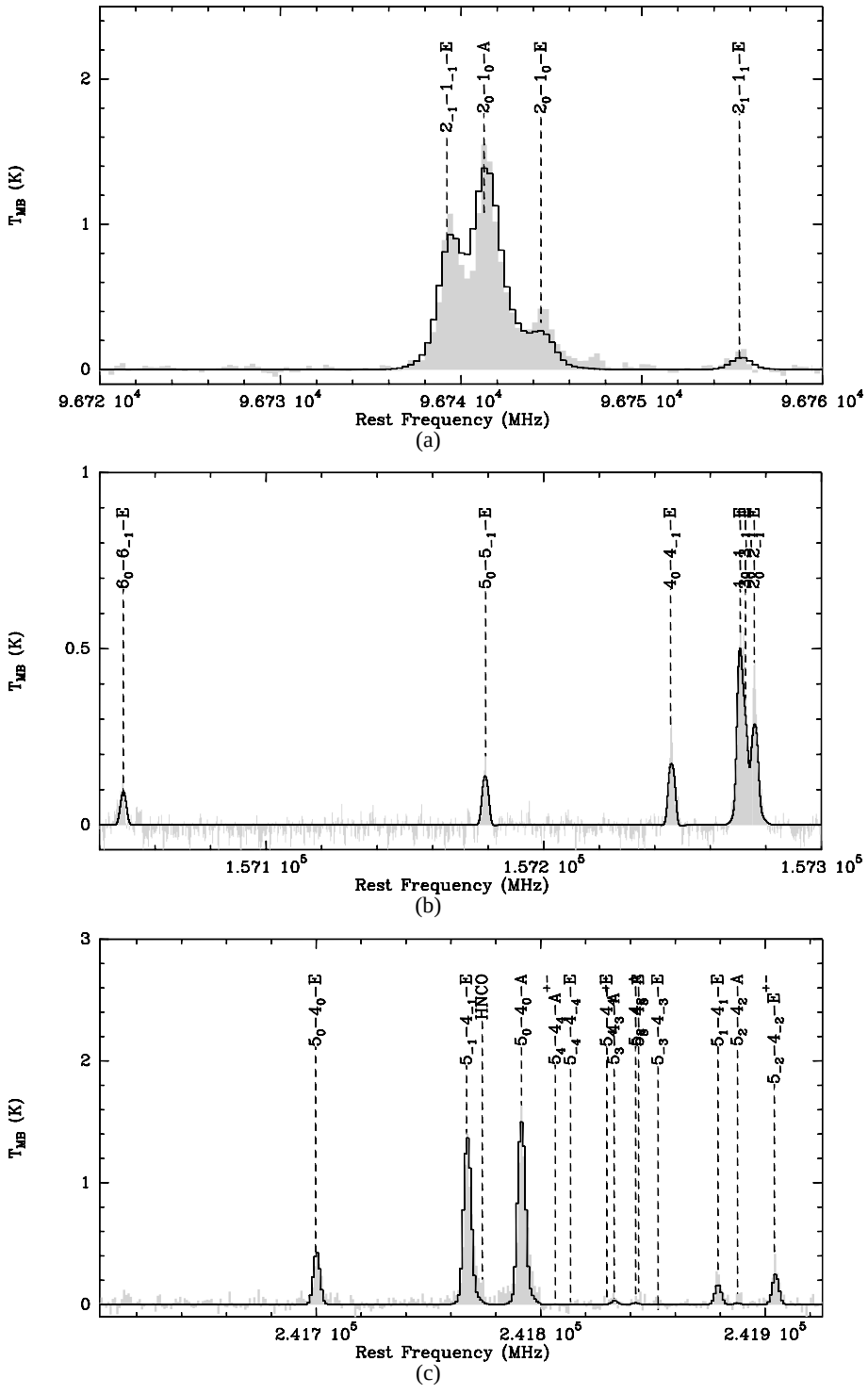

Fig. 29. Spectra toward IRAS 23139+5939 taken with the IRAM 30 m telescope. The 1 mm and 2 mm data are smoothed to the resolution of the 3 mm spectra **a)**. All observed lines are labelled. The synthetic spectra resulting from the fit are overlaid in black.